Structure of the nucleus ^{114}Sn using gamma-ray coincidence data

Sean Benjamin Oates

Thesis presented in fulfilment of the requirements for the degree of Master of Science at Rhodes University

Supervisor

Prof. D. G. Roux

Department of Physics and Electronics

Rhodes University

August 31, 2015

Abstract

An investigation into the decay scheme of ^{114}Sn was carried out via the $^{114}_{48}Cd_{66}(^{3}He,3n)^{114}_{50}Sn_{64}$ reaction at a lab energy of 25MeV, i.e. a fusion evaporation reaction, using the AFRODITE array in conjunction with a "wall" of neutron detectors at iThemba LABS. Several new levels were added to the decay scheme of ^{114}Sn via the study of $\gamma-$ray coincidence data. Spin and parity could be assigned to the new levels where possible using a combination of Directional Correlations from Oriented states (DCO) and polarisation anisotropy analysis. The so-called Amsterdam band, a $K^{\pi} = 0^{+}$ band known to be present in the even $^{112-118}$Sn isotopes, was observed, and its configuration and alignment properties are discussed in the context of the particle rotor model.

Acknowledgements

I would like to thank iThemba LABS for giving me the opportunity to analyse the data collected in this experiment. They were an instrumental part of this project. In particular I would like to thank Pete Jones for his consistent guidance and advice. In addition the NRF for their funding which enabled me to continue my studies and take on this opportunity. I am honoured by their support and faith in me.

Professor David. G. Roux who has been with me throughout this journey. I am indebted to you for the role you have played and for your tireless commitment to me and this project.

I would like to thank the staff of the Rhodes University Physics and Electronics Department who have all contributed to my achievements over the past few years.

Also, a big thank you to my friends and fellow students for lending a helping hand in difficult times.

And finally, Mum and Dad I cannot begin to express how much I appreciate all you have done to get me to this point. You set me on this path so long ago and have been a constant rock of support throughout it all. I truly am blessed to have you behind me in everything I do.

Contents

Introduction **8**

Chapter 1 Nuclear Theory **10**

Nuclear Shell Model 10

Deformed Shell Model or Nilsson Model 12

Potential Energy Surfaces 18

Collective Excitations 19

Vibrational Excitations 20

Rotational Excitations 20

Particle Rotor Model 20

Alignment and Backbending 22

Angular Distribution 23

Directional Correlation through Oriented states Analysis 26

Polarisation Anisotropy Analysis 26

Chapter 2 Experiment **29**

Experimental Setup 29

Chapter 3 Results **34**

Level Scheme 34

Positions of the new γ rays 35

Spin and Parity 43

Chapter 4 Discussion **52**

Chapter 5 Conclusion **58**

Bibliograpy **60**

List of Figures

1 On the left hand side are the pure SHO shells. The centre levels show the effect of an l^2 term being added to the SHO levels. The levels on the right hand side show the effect on the "intermediate" levels when the spin orbital interaction is taken into account [13]. 12

2 The Lund convention. Values of γ=0° and -120° correspond to prolate shapes, while γ=-60° and 60° correspond to oblate shapes. Collective excitations are found in the region -60° $\leq \gamma \leq$0° [14]. 14

3 Nilsson diagram for protons, 50$\leq$ Z $\leq$ 82 (ε_4=ε_2^2/6) [5]. The Fermi level at deformation of β_2 = 0.26 for protons in ^{114}Sn is near the region of the 1/2[431]$^+$ orbital and 9/2[404]$^+$ orbital. 16

4 Nilsson diagram for neutrons, 50$\leq$ N $\leq$ 82 (ε_4=ε_2^2/6) [5]. The Fermi level at deformation of β_2 = 0.26 for neutrons in ^{114}Sn is near the region of the 5/2[413]$^+$ orbital and 5/2[532]$^-$ orbital. 17

5 Panel (a) shows how the collective rotation angular momentum vector R couples with the orbital angular momentum j in the Deformation Aligned (DAL) case. K=Ω is a constant of the motion. Panel (b) shows the Rotation Aligned (RAL) case where j_x is a constant of the motion [14]. 22

6 Shows that an increase in alignment occurs for lower rotational frequencies after a backbending has occurred [9]. 23

7 Angular distribution for γ rays with different multipolarities [9]. 25

8 Schematic set-up for the ^{114}Cd(^{3}He,3n)^{114}Sn experiment [11]. 30

9 AFRODITE array setup used in this experiment. The beam enters the array from the right hand side of the image. The image shows the clover detectors in the θ = 90° ring and the θ = 135° ring about the beam line and also the bank of neutron detectors placed 1.93 m downstream of the array at θ = 0° about the beamline. 31

10 Schematic of the clover detectors used in the AFRODITE array. Image a) shows the entire clover detector with the BGO anti-compton shielding shown in yellow and on the right hand side is the liquid nitrogen dewar shown in pale blue. Image b) shows a cross section though the HPGe crystals of image a) along the dotted line. Image c) is a 3D representation of the HPGe crystals in their four-leaf clover arrangement. 32
11 Level scheme of ^{114}Sn. Arrow widths are proportional to γ ray intensity and all energies are in keV. 34
12 Coincidence spectrum gated on the 444-keV γ ray in the top panel along with the coincidence spectrum gated on the 261-keV γ ray in the bottom panel. . 36
13 Level scheme showing the levels present in ^{115}In [16] seen in the data. The red circles highlight the 444-keV γ ray and a 261-keV γ ray in the level scheme. 36
14 Spectrum gated on the 1284-keV γ ray. γ rays labelled with an asterisk (*) are significant contaminants in the spectrum. The 511-keV peak is attributed to electron-positron annihilation. 38
15 Coincidence spectrum gated on the 429-keV γ ray. 39
16 Coincidence spectrum gated on 272-keV γ ray. 40
17 Coincidence spectrum gated on the 322-keV γ ray. 41
18 Coincidence spectrum gated on the the 320-keV γ ray. 41
19 Coincidence spectrum gated on the 1160-keV γ ray. 43
20 Measured value of R_{DCO} for the 1284-keV γ ray shown with error bars, plotted as a function of mixing ratio, δ. The curved broken lines are labelled with their corresponding spin sequence. 49
21 Measured value of R_{DCO} for the 429-keV γ ray shown with error bars, plotted as a function of mixing ratio, δ. The curved broken lines are labelled with their corresponding spin sequence. 50
22 Nilsson diagram [5] for protons, $50 \leq Z \leq 82$ ($\varepsilon_4 = \varepsilon_2^2/6$) 54

23 Total Routhian surface calculations for ^{118}Sn at $\hbar\omega$=0.00 MeV (top left), $\hbar\omega$=0.10 MeV (top right), $\hbar\omega$=0.20 MeV (bottom left) and $\hbar\omega$=0.50 MeV (bottom right). Energy contours are at 200-keV intervals [21]. 55

24 Experimental alignment plots for Band 4 in ^{114}Sn seen as filled circles, plotted with the alignment plot for the Amsterdam band in ^{118}Sn, hollow circles, as seen in Wang *et al.* [21]. The Harris parameters used are J_0=15 $\hbar^2$ MeV^{-1} and J_1=25 $\hbar^4$ MeV^{-3}. 56

List of Tables

1 Table of new decays in level scheme, shown in order of ascending energy of the γ ray. 35

2 Table of DCO ratio values and errors for all transitions in the level scheme, grouped by the gating transition used to determine the DCO ratio. 45

3 Table of polarisation anisotropy values and errors for all decays in the level scheme, grouped by the gating transition used to calculate the polarisation value for the specified γ ray. ΔQ=0.02 for all values Q. 46

4 Extract from Table 2 showing DCO ratio values for the newly added decays in the level scheme, shown in order of ascending energy of the γ ray. 47

5 Extract from Table 3 showing the polarisation anisotropy values for newly added decays in the level scheme, shown in order of ascending energy of the γ ray. 47

Introduction

Jones *et al.* proposed [11] the $^{114}_{48}Cd_{66}(^{3}He,n)^{116}_{50}Sn_{64}$ two proton stripping experiment. The experiment was proposed as a continuation of the ^{100}Ru and ^{150}Sm studies carried out previously [3] as these were also two proton stripping experiments. Two proton stripping reactions ensure that paired protons are transferred to the target nucleus and therefore zero spin is transferred in the reaction. To ensure that states with zero orbital angular momentum are populated, neutron detection at $\theta = 0^\circ$ to the beam line was also used in the experiment. If neutrons are detected at $\theta = 0^\circ$ this means that the orbital angular momentum of the final state nucleus must be 0. The orbital angular momentum of the nucleus ℓ and the angle θ at which outgoing particles are scattered are directly related by [9]

$$\ell \cong 8 \sin \frac{\theta}{2}$$

If $\ell = 0$ states are populated then the 0^+_2 excited state, which is simply the second 0^+ excited state of ^{116}Sn should be populated. The 0^+_2 excited state is interesting from the point of view of double beta decay. Therefore studying the 0^+_2 excited state leads to a better understanding of double beta decay better. Double beta decay is very rare but some nuclei that do undergo it are ^{100}Ru, ^{150}Sm and ^{116}Sn with half lives of 7.1(4)x10^{18}, 7.8(7)x10^{18} [11] and 3.0(2)x10^{19} years [1] respectively.

Double beta decay is expected to occur in two different ways. The first is the two-neutrino double-beta decay ($\beta\beta(2\bar{\nu})$) in which 2 electron antineutrinos and 2 electrons are emitted from a nucleus that has undergone a decay from an initial state of (Z, A) to a final state of (Z+2, A). The emission of the 2 electron antineutrinos occurs whether or not they are their own antiparticles. The second type of double beta decay is the neutrinoless double beta decay ($\beta\beta(0\nu)$) which has never been observed. ($\beta\beta(0\nu)$) could only occur if neutrinos are their own antiparticles and therefore an observation of ($\beta\beta(0\nu)$) would establish that neutrinos are Majorana particles and that $\nu \equiv \bar{\nu}$ [1].

Upon investigation of the data from the experiment, it was found that the reaction had produced ^{114}Sn instead of ^{116}Sn as proposed. We therefore intend to add to the previously existing level schemes for ^{114}Sn by using a series of experimental and analytical techniques, such as Directional Correlation of Oriented states (DCO) analysis and polarisation anisotropy analysis [9] on the decays observed in the data. These two methods combined will, in most cases, allow for the determination of the spin and parity of the states observed in the decay scheme.

There are several compelling reasons to study the even tin isotopes. Firstly, they are known to exhibit the phenomenon of shape coexistence. This means that the nucleus may have different deformations at the same rotational frequency. At large rotational frequency they are also seen to be $\gamma-$soft and therefore the nucleus does not have a fixed $\gamma-$deformation, but instead oscillates between all possible values of $\gamma-$deformation. Secondly, ^{114}Sn is known to have a spherical ground state as it is doubly even, and it also has a deformed 0_2^+ excited state as the band head of the Amsterdam band [22]. The Amsterdam band is a band that is known to be present in all the even $^{112-118}$Sn isotopes. The band has a 2-particle-2-hole configuration and it is also known that backbending occurs in the high spin states of the band due to the alignment of 2 quasineutrons. Finally, most of the states found in ^{114}Sn are shell model states and therefore do not represent any collective motion.

In Chapter 1 of the thesis the relevant theory required to understand the analytical techniques will be discussed and explained. Chapter 2 will be a description of the apparatus used in the experiment and the AFRODITE array. In Chapter 3 we will discuss the levels observed in the level scheme, this includes the spin and parity assignments of newly added levels and the energies of the newly observed decays. Chapter 4 then discusses the configurations and shapes of the levels observed in ^{114}Sn. Chapter 5 will summarise the thesis and suggest the need for future experiments or further investigations.

Chapter 1. Nuclear Theory

Nuclear Shell Model

Most nuclei are not simply one or two interacting nucleons, but in fact are made up of many interacting bodies. The nuclear shell model tries to simplify this by treating individual nucleons as if they are in a mean field created by all the other interacting nucleons. If the mean field takes the form of a Woods-Saxon potential [13] then this gives rise to the spherical nuclear shell model, while a deformed mean field results in the deformed nuclear shell model. The Woods-Saxon potential can be expressed as

$$V(r) = \frac{-V_0}{1 + exp[\frac{(r-R)}{a}]}$$

where V_0 defines the depth of the potential while r is the radial distance from the centre of the potential well, and a is a parameter that determines how quickly the potential rises to zero. R is the value of the radius at which point the potential has become half of V_0.

The nuclear shell model is one in which the nucleons occupy shells within the nucleus. Each shell can contain only a certain number of nucleons before it is full, and adding another nucleon to the nucleus would result in it having to occupy a position in the next shell as stated by the Pauli exclusion principle. When a nucleus contains only full shells for either its protons or neutrons it is said to be magic and is called a single-closed-shell nucleus, while a nucleus with full proton and neutron shells is said to be a doubly magic nucleus and is called a doubly-closed shell nucleus. The magic numbers are the total number of protons or neutrons required to fill each subshell, and for protons and neutrons are as follows,

$$Z = 2, 8, 20, 28, 50, 82$$

$$N = 2, 8, 20, 28, 50, 82, 126$$

Nuclei that are doubly magic are highly stable nuclei. When a nucleus contains a nucleon number that is a magic number +1 nucleon it can be thought of having all full shells except for one shell that only contains one nucleon.

Since spherical symmetry occurs, the Schrödinger equation [13] can be written as

$$\left(-\frac{\hbar^2}{2M}\frac{1}{r}\frac{d^2}{dr^2}r + \frac{\hbar^2 l(l+1)}{2Mr^2} + V(r) - E \right) R(r) = 0$$

Where M is the average nucleon mass, r is the radius of the nucleus, l is the angular momentum, $V(r)$ is the nuclear one-body potential, E is the energy of the one-body state and $R(r)$ is the radial wave function. When a harmonic oscillator potential or an infinite square well potential is used for the $V(r)$ term, this results in the single particle subshells shown in Figure 1 [13]. The levels at the centre of Figure 1 are the single particle subshells for a more realistic Woods-Saxon potential.

These subshells shown the middle of Figure 1 [13] do not quite correspond with the magic numbers stated earlier and this can be achieved by introducing a spin-orbit term to the potential used in Schrödinger equation. The addition of this term produces the subshell energy levels seen on the right hand side of Figure 1. These energy gaps correspond perfectly with the earlier stated magic numbers.

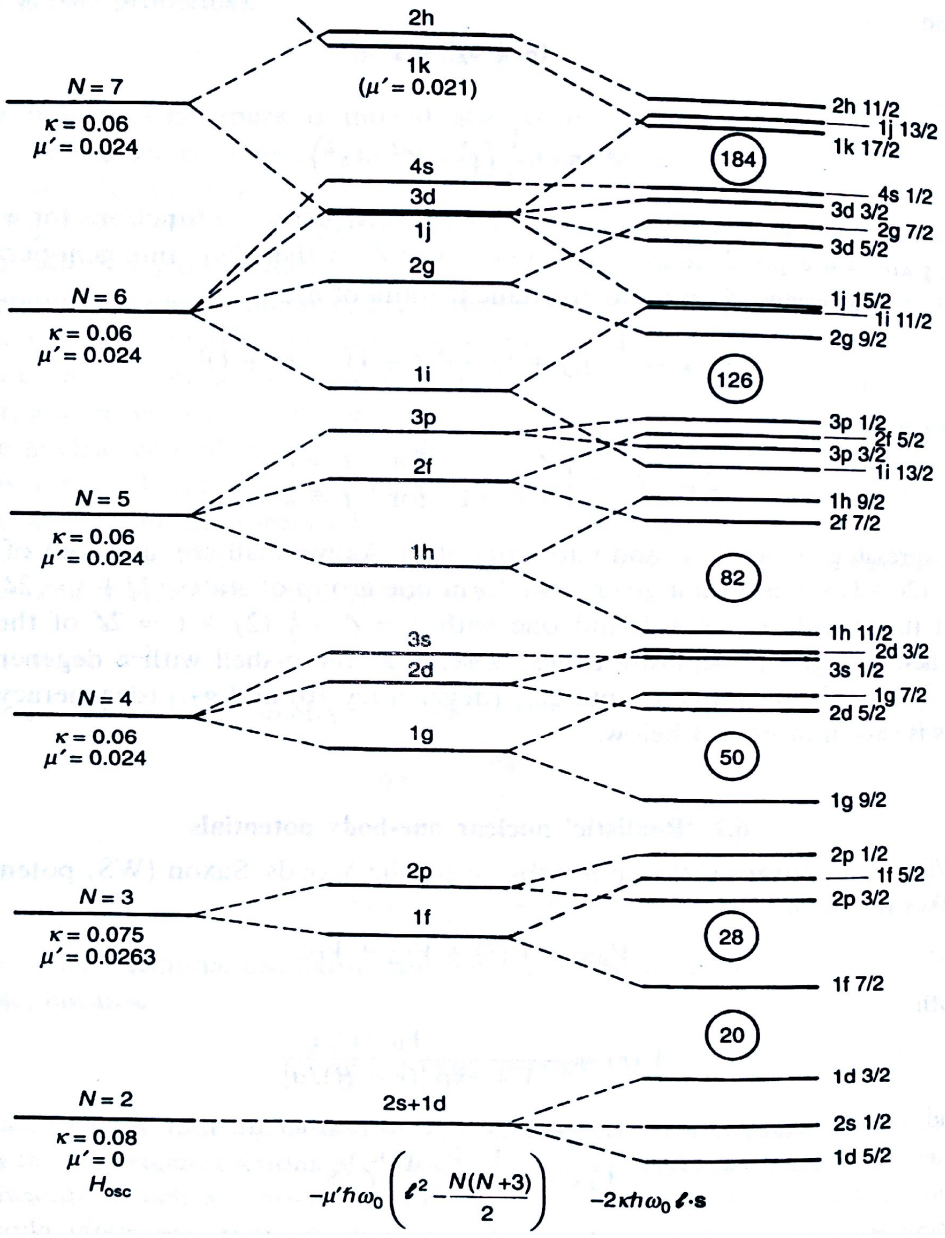

Figure 1: On the left hand side are the pure SHO shells. The centre levels show the effect of an l^2 term being added to the SHO levels. The levels on the right hand side show the effect on the "intermediate" levels when the spin orbital interaction is taken into account [13].

Deformed Shell Model or Nilsson Model

Nuclei with many valence nucleons outside a closed shell tend to have a deformed mean field. Deformed nuclei commonly have axial symmetry or a triaxial shape. The shape of the nucleus can be parameterized by

$$R(\theta,\phi) = R_0\left[1 + \sum_{\lambda\mu} \alpha_{\lambda\mu}(t)\cdot Y_{\lambda\mu}(\theta,\phi)\right]$$

where $R(\theta,\phi)$ is the length of the radius vector from the origin to the surface. If the $\alpha_{\lambda\mu}$(t) term is not time dependent then the resulting nuclear shape is static but deformed. $Y_{\lambda\mu}(\theta,\phi)$ represents the spherical harmonics of the nucleus and describes the expansion of the nuclear surface when vibrational excitations occur.

The degree to which a nucleus is deformed can be described by several quadrupole deformation parameters. One such parameter is the Nilsson deformation parameter ϵ_2. Other parameters can be determined from the Nilsson deformation parameter such as the Woods-Saxon deformation parameter β_2. δ can also be used to describe the deformation of the nucleus. These deformation parameters can be approximated by [23]

$$\epsilon_2 \cong \left(\frac{1176}{A^{\frac{7}{3}}E(2^+)}\right)^{\frac{1}{2}} \cong 0.944\beta_2 - 0.122\beta_2^2$$

$$\beta_2 \cong \left(\frac{1225}{A^{\frac{7}{3}}E(2^+)}\right)^{\frac{1}{2}}$$

$$\delta \cong \frac{R_3 - R_\perp}{R}$$

where R is the average radius of the nucleus, R_3 is the the semi-major axis, $R_\perp$ is the semi-minor axis, A is the mass number of the nucleus in question and E(2^+) is the energy of the 2^+ collective state (first excited state) of the even-even nucleus measured in MeV.

There are two types of axially symmetric deformed shapes, prolate deformed and oblate deformed. A prolate deformed nucleus is elongated along the symmetry axis, and will have a value of $\beta_2 > 0$. Oblate deformation is a flattening of the nucleus along the symmetry axis

and will have a deformation value of $\beta_2 < 0$.

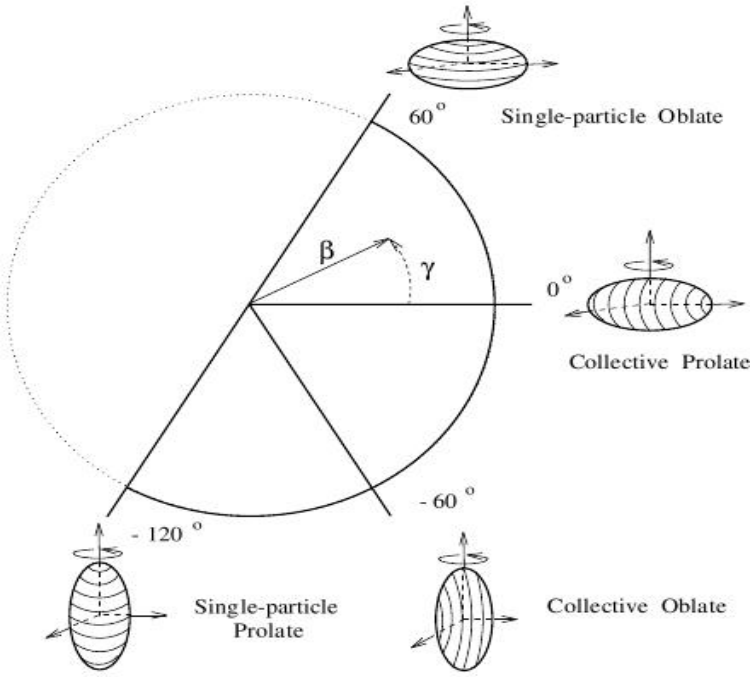

Figure 2: The Lund convention. Values of γ=0° and -120° correspond to prolate shapes, while γ=-60° and 60° correspond to oblate shapes. Collective excitations are found in the region -60° $\leq \gamma \leq$0° [14].

Nuclei can also have a deformation that is not symmetrical about any axis and this results in a triaxial shape, measured by a triaxiality parameter γ.

When symmetry is broken, spherical states become mixed and the degeneracy of the j-orbitals is lifted, therefore j and ℓ can no longer uniquely identify the nuclear states. Therefore "Nilsson" quantum numbers must be introduced, namely N which is the simple harmonic oscillator shell number, n_z which is the number of nodes for axial vibrations (in 3 dimensions, this is taken along the z-axis), Λ which is the projection of l along the z-axis, and Ω which is the projection of j along the z-axis. These states are labelled as $[Nn_3\Lambda]\Omega^\pi$ but are only good quantum numbers in the asymptotic limit of large deformations [13]. Only Ω and π are good quantum numbers for intermediate deformations as the Nilsson orbitals become mixed.

Nilsson diagrams are a plot of the single-particle energy levels in a deformed potential.

Each state in the Nilsson diagram is labelled with asymptotic quantum numbers as $[Nn_3\Lambda]\Omega^\pi$ [12]. Nilsson diagrams for protons and neutrons between 50 and 82 are shown in Figures 3 and 4 respectively. β_2=0.26 for the K $^\pi = 0^+$ band in ^{114}Sn.

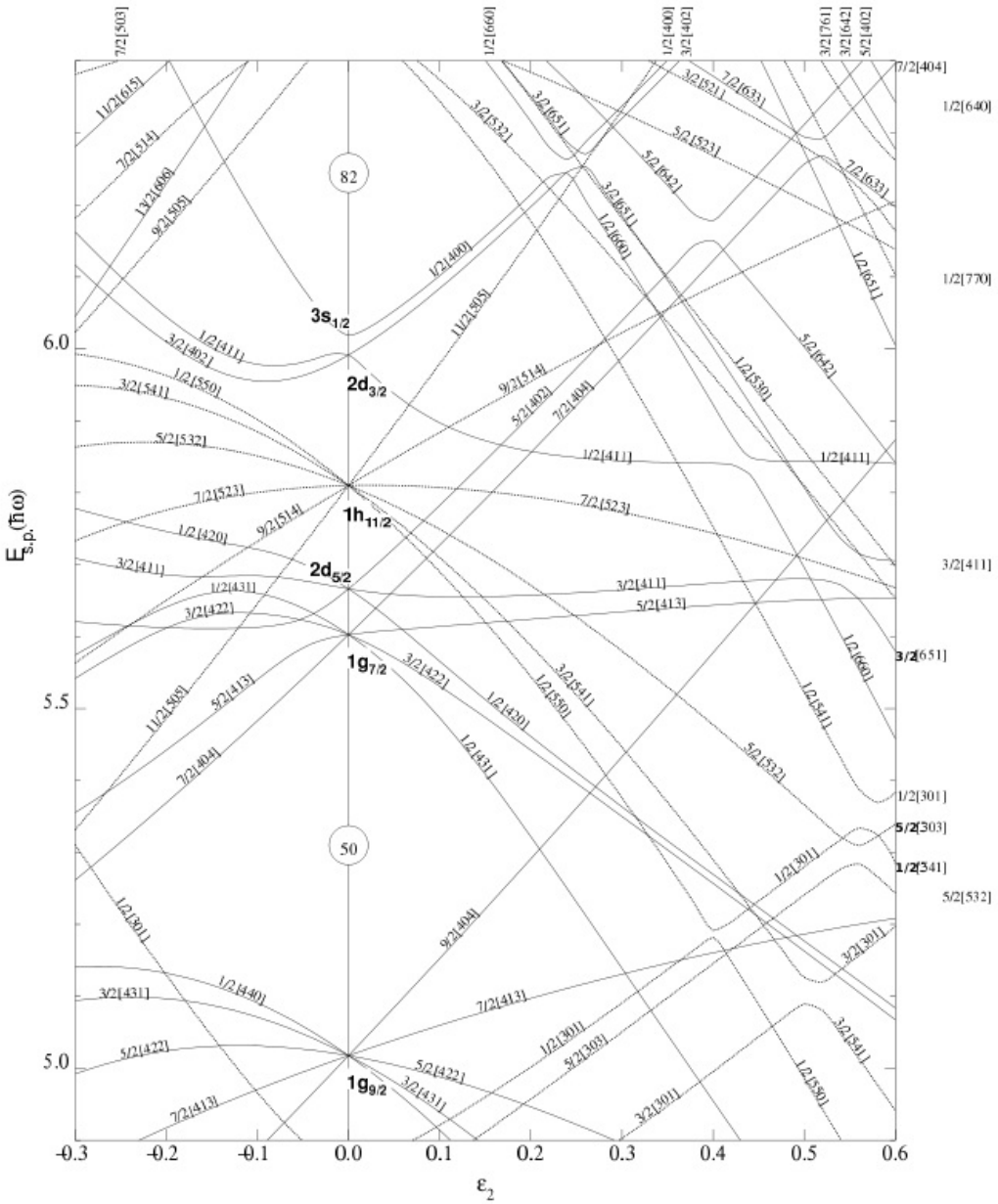

Figure 3: Nilsson diagram for protons, $50 \leq Z \leq 82$ ($\varepsilon_4 = \varepsilon_2^2/6$) [5]. The Fermi level at deformation of $\beta_2 = 0.26$ for protons in ^{114}Sn is near the region of the $1/2[431]^+$ orbital and $9/2[404]^+$ orbital.

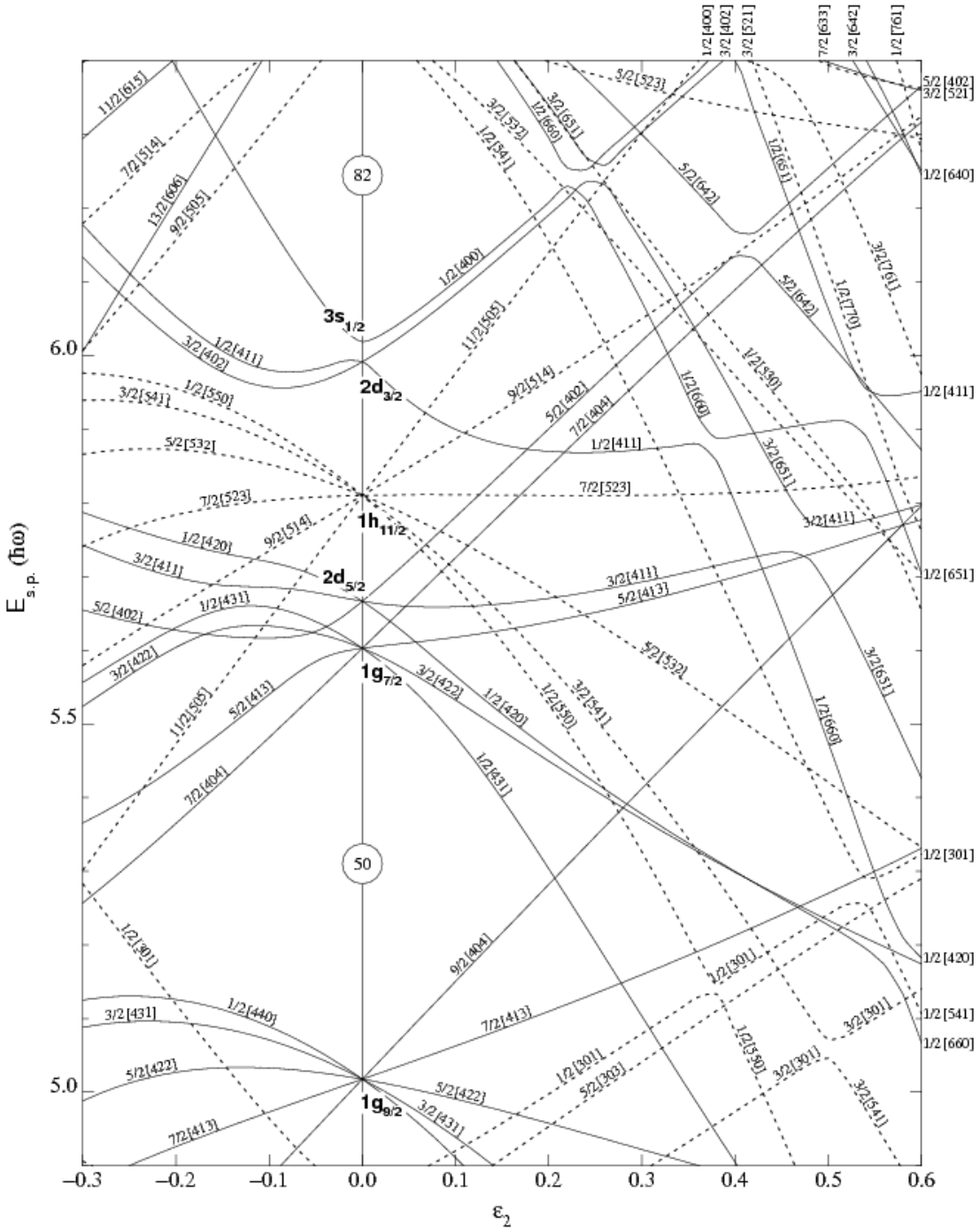

Figure 4: Nilsson diagram for neutrons, $50 \leq N \leq 82$ ($\varepsilon_4 = \varepsilon_2^2/6$) [5]. The Fermi level at deformation of $\beta_2 = 0.26$ for neutrons in ^{114}Sn is near the region of the $5/2[413]^+$ orbital and $5/2[532]^-$ orbital.

When the deformation of the nuclei becomes very large then the only good quantum numbers are Ω and π with each Ω orbital able to hold only 2 nucleons of the same type.

Even-even nuclei are found to have a configuration in which all nucleons are paired and therefore have a vacuum configuration for the ground state. Odd-even nuclei have a ground state associated with the occupation of one Nilsson orbital by the valence nucleon. Odd-odd nuclei have ground state associated with the occupation of one Nilsson orbital by its valence neutron as well as the occupation of one Nilsson orbital by its valence proton. This ground state may be deformed in which case there may be an associated collective rotation of the nucleus. Collective rotation involves the rotation of the intrinsic shape of the nucleus as a whole. Excited states are also associated with Nilsson orbitals and therefore each excited state may also rotate collectively if it is deformed [23].

Potential Energy Surfaces

In the Strutinsky procedure (shell correction procedure) it is known that on average, the long-range behaviour of the nuclear binding energy as a function of the nuclear charge and size is well reproduced by the liquid-drop model. The Strutinsky procedure suggests that on average the liquid drop model also adequately describes the deformation [13]. This therefore requires that on average the total energy has the same distortion dependence as that of a liquid drop. To ensure this dependence, an average energy can be replaced by a liquid-drop energy in the total nuclear energy [13].

Strutinsky compares the actual discrete level structure g, given by

$$g(e) = \sum_{\nu} \delta(e - e_v)$$

with a smeared level density $\tilde{\mathrm{g}}(e)$. Where e_v is the single-particle energy level and $\tilde{\mathrm{g}}(e)$

is the smoothed level density. This defines the shell energy as

$$E_{sh} = 2\sum e_v - 2\int e\tilde{\mathrm{g}}(e)\mathrm{d}e$$

For an even nucleus the total energy is therefore given by

$$E_{tot} = E_{L.D.} + E_{sh}(\text{protons}) + E_{sh}(\text{neutrons})$$

Potential Energy Surface (PES) calculations are used to determine the total energy of the nucleus, using the shell correction procedure, as a function of nuclear deformation, rotational frequency and the nucleon configuration. In order to plot a PES diagram the calculation uses a particular nucleon configuration and rotational frequency, then a minimum in the total energy is found for all possible deformations. The position of the minimum in the PES diagram may reveal information about the shape and deformation of the nucleus. If several minima are present in one diagram this represents a special case of shape coexistence. By repeating the calculation for several rotational frequencies, several PES surface diagrams are produced. This allows the shape of the nucleus to be analysed over several different rotational frequencies [13].

Collective Excitations

The nuclear shell model only accounts for the motion of independent nucleons under the influence of a mean field. However, as more and more valence nucleons are added beyond the magic numbers the nuclear shell model does not adequately describe the nucleus. The nuclear shell model can however be extended to include the effect of residual interactions within the nucleus. These residual interactions account for the deformations observed in nuclei. When a nucleus becomes deformed, collective excitations must also be considered. Collective excitations can be divided into two types of collective motion, vibrational excitations and

rotational excitations.

Vibrational Excitations

Vibrational excitations are characterised by a spherical equilibrium shape with shape varying repetitively about that equilibrium shape. Vibrational excitations occur in different modes, namely monopole (λ=0), dipole (λ=1), quadrupole (λ=2) and octupole (λ=3). The quadrupole vibrations can be broken into two modes, namely, β vibrations (K=0) and γ vibrations (K=2) where K is the projection of the total angular momentum on the symmetry axis. If the z-axis is the elongation axis, in β vibrations the x-y cross-section of the nucleus remains circular, while the x-y cross-section of γ vibrations changes to an elliptical shape. Vibrational excitations and the particular mode can be identified within a nucleus by looking at groups or clusters of levels within the bands of the level scheme of the nucleus.

The vibrations of the nucleus can be described using the same set of dynamic shape parameters that describe the nuclear shape. We have already seen that $\alpha_{\lambda\mu}$ can be constant with time causing a nucleus to be deformed, but $\alpha_{\lambda\mu}$ can also be time dependent, in which case the nucleus vibrates about a spherical equilibrium shape.

Rotational Excitations

Rotational excitations are characterized by the nucleus rotating when deformed as a whole about an axis within the nucleus. Rotational excitations can be identified by the bands that are present in the level scheme. An example of a rotational bad would be the even-spin, positive parity Amsterdam band connected by stretched E2 transitions found in the even $^{112-118}$Sn nuclei.

Particle Rotor Model

When we solve the Time Independent Schrödinger Equation (TISE) with the full Hamiltonian

$$H = H_{sp} + H_{rot}$$

where H_{sp} is the deformed single-particle Hamiltonian and H_{rot} is the rotation Hamiltonian. Total energy is given by

$$E_{IK} = |e_v - \lambda| + \frac{\hbar^2}{2\mathcal{J}}\Big[I(I+1) - K^2\Big], K \neq \frac{1}{2}$$

where the single-particle energy is counted relative to the Fermi level energy λ. e_v are the single-particle energies, $\mathcal{J}$ is the moment of inertia, I is the total spin of the nucleus and K is the projection of the total angular momentum on the symmetry axis. As $I \geq K$, the spins I=$K, K+1, K+2$,... are observed [13].

For odd-A nuclei when a collective rotation occurs, the collective rotation axis R and the orbital angular momentum j of a single valence nucleon couple together in the particle rotor model. This coupling occurs as the valence nucleon is rotating about a doubly-even rotating core. A Coriolis force therefore acts on the valence nucleon due to the rotating core nucleus. There are two main limits to this coupling, namely, Deformation Aligned coupling (DAL) and Rotation Aligned coupling (RAL). DAL is when the spin of the odd nucleon is strongly coupled to the deformation, while RAL is when the coupling between spin of the odd nucleus and the core is at the weak-coupling limit and results in the spin of the odd nucleus being aligned with the rotation axis [14]. Figure 5 shows how the orbital angular momentum and the rotation couple in the the two cases of DAL and RAL.

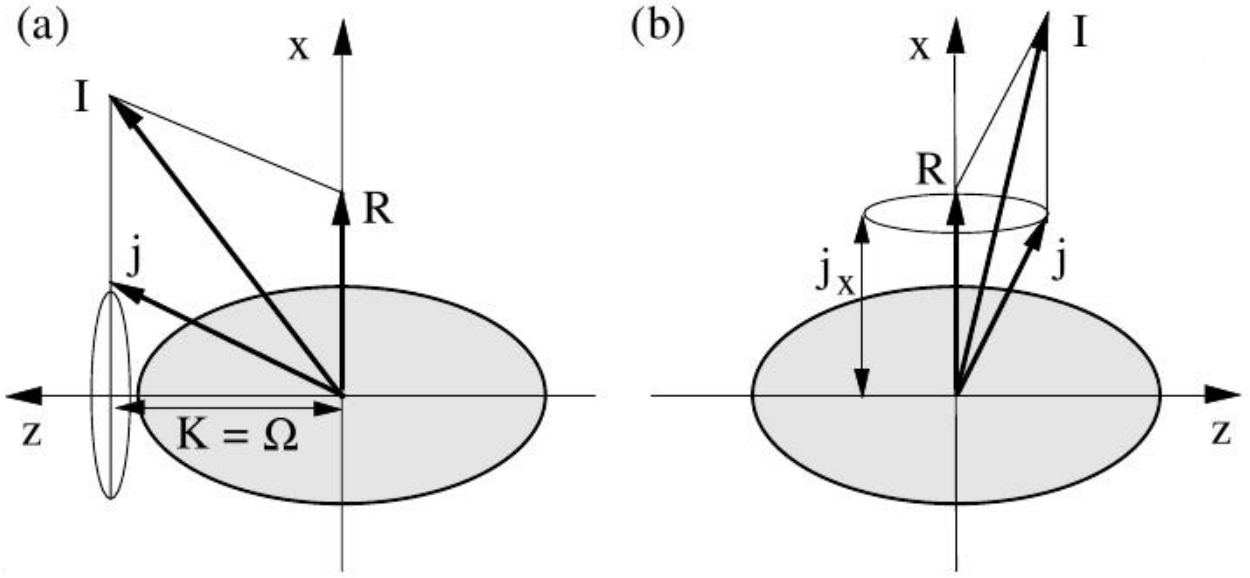

Figure 5: Panel (a) shows how the collective rotation angular momentum vector R couples with the orbital angular momentum j in the Deformation Aligned (DAL) case. K=Ω is a constant of the motion. Panel (b) shows the Rotation Aligned (RAL) case where j_x is a constant of the motion [14].

DAL is favoured when the nucleus is very deformed and if j is large then DAL occurs only for the high-Ω orbitals. These orbitals are known as deformation aligned orbitals and bands that are built on these orbitals are deformation aligned bands. RAL is favoured by nuclei that have smaller deformation and occurs when the odd nucleon occupies a low-Ω orbital. These orbitals are known as rotation aligned orbitals and the bands built off of them are rotation aligned bands. These low-Ω orbitals are strongly affected by the Coriolis force.

Alignment and Backbending

At high enough rotational frequencies the Coriolis force acting within a nucleus becomes strong enough to break apart valence nucleon pairs. When the pair is broken, the nucleons' spins align with the rotation axis of the entire nucleus and therefore contribute to the angular momentum.

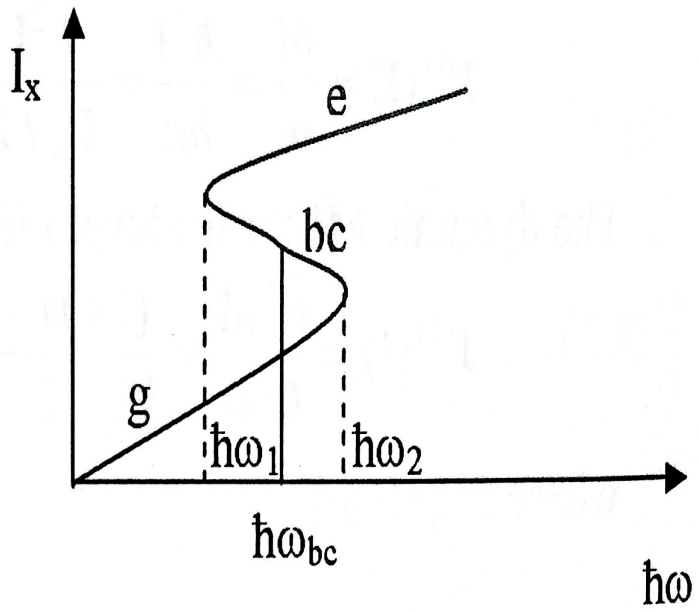

Figure 6: Shows that an increase in alignment occurs for lower rotational frequencies after a backbending has occurred [9].

Figure 6 shows a theoretical plot of the aligned angular momentum I_x (the projection of the angular momentum along the rotation axis) versus the rotational frequency $\hbar\omega$. Figure 6 shows backbending occurring at the point labelled 'bc'. This is the point where a nucleon pair is broken and their spins have aligned with the rotation axis. This results in an increased alignment, I_x, but at a slightly lower rotational frequency, $\hbar\omega_1$. The values of the alignment and the bandcrossing frequency $\hbar\omega_{bc}$ are important values as they allow us to determine the configuration of the excited state [9].

Angular Distribution of γ rays

In a nuclear reaction a compound nucleus becomes fully oriented due to the angular momentum imparted to it from the projectile. The angular momentum is aligned perpendicular to the direction of the incoming particle. The γ rays that are emitted from from the de-excitation of the nucleus have an angular distribution that takes the form of

$$W(\theta) = 1 + \sum_{k-even} \alpha_k A_K(I_i, L, L', I_f) P_k(\cos\theta)$$

where $L' = L + 1$, α_k are attenuation factors between 0 and 1, A_K are theoretically calculated coefficients which depend on the initial and final nuclear spins I_I and I_f as well as the multipolarity of the radiation L [9]. θ is the angle about the beamline in which the γ ray is emitted.

Therefore the angular distribution for a fully aligned stretched dipole is given by

$$W(\theta) = A_0 + A_2 P_2(\cos\theta) = A_0\big[1 + a_2 P_2(\cos\theta)\big]$$

and the angular distribution for a fully aligned stretched quadrupole is given by

$$W(\theta) = A_0 + A_2 P_2(\cos\theta) + A_4 P_4(\cos\theta) = A_0\big[1 + a_2 P_2(\cos\theta) + a_4 P_4(\cos\theta)\big]$$

where A_0 is proportional to the intensity of the γ ray. a_2 is negative in the case of a stretched dipole transition and is positive for a stretched quadrupole transition and a_4 is negative for a stretched quadrupole transition. In the case of stretched dipoles $W(\theta)$ is a maximum at 90° whereas stretched quadrupole transitions have a maximum angular distribution at 0° and 180° [9].

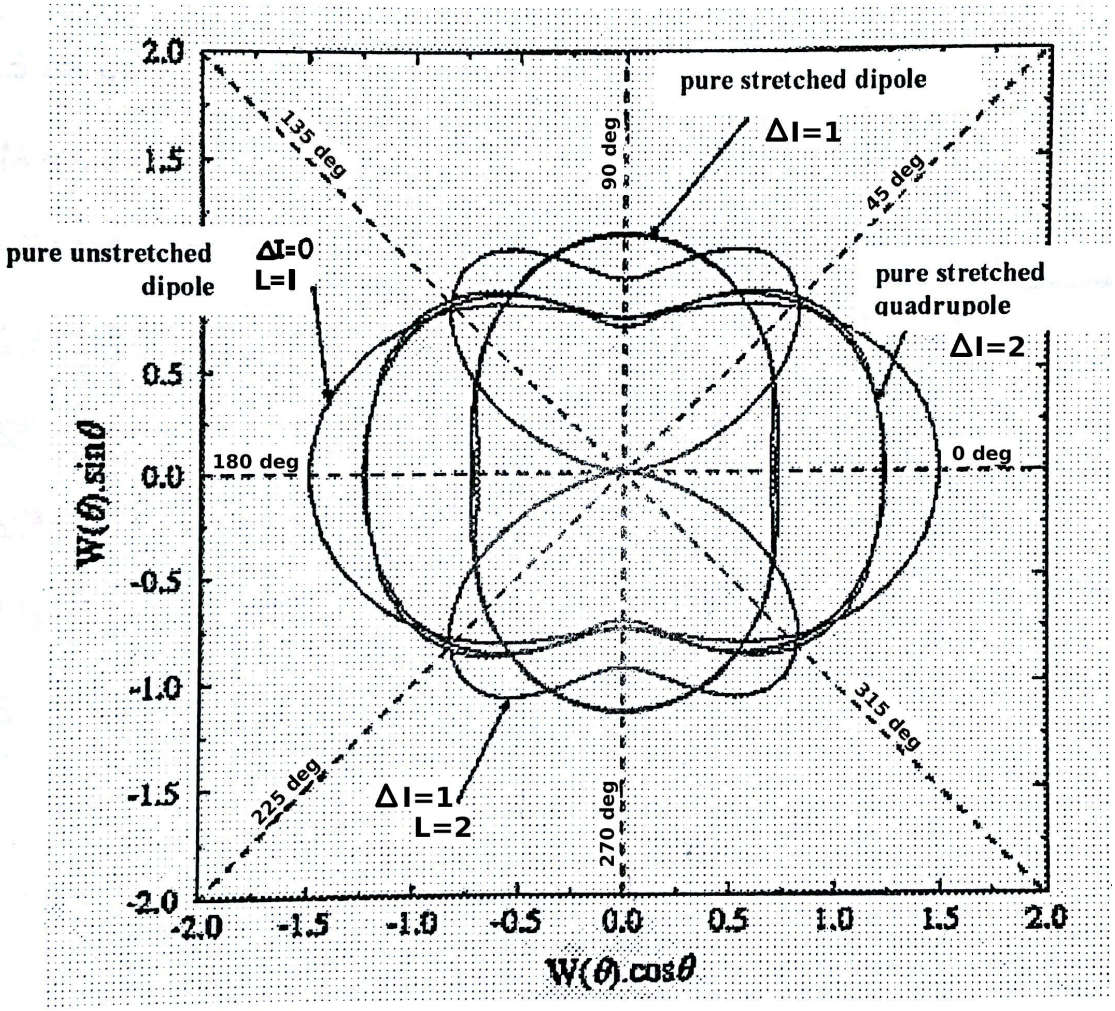

Figure 7: Angular distribution for γ rays with different multipolarities [9].

Figure 7 shows how the angular distribution varies for γ rays with different multipolar-

ities, with pure stretched dipole transitions having a maximum at 90° and pure stretched quadrupole transitions having a maximum at 0° and 180°.

Directional Correlation through Oriented states (DCO) Analysis

The DCO ratio, R_{DCO}, is a measure of the number of γ rays that are emitted at 90^o and 135^o to the beam line, where one γ ray is emitted at 90^o while the other γ ray is emitted at 135^o. The R_{DCO} value generally allows the multipolarity of γ rays to be determined when the γ ray is emitted from an oriented nuclear state [9]. The multipolarity of the γ ray is determined by comparing the measured R_{DCO} value with theoretically calculated R_{DCO} values for different multipole orders.

The value of measured R_{DCO} is given by

$$R_{DCO} = \frac{R(90°, 135°, 45°)}{R(135°, 90°, 45°)}$$

where R(90°,135°,45°) represents the intensity of a γ ray detected in a 90^o clover with a gate set on a 135^o clover, and R(135°,90°,45°) represents the intensity of the same γ ray detected in a 135^o clover with a gate set on a 190^o clover. 45° is the azimuthal angle between the detectors. Values of R_{DCO} for stretched λ=2 transitions are expected to be 1.0 while R_{DCO} for stretched λ=1 transitions are expected to be 0.6 [17]. Mixed transitions can have an R_{DCO} that is anywhere between 0.5 and 1.5 [17], and therefore in order to characterize the type of transition the R_{DCO} value must be compared to theoretically calculated values.

Polarisation Anisotropy Analysis

The polarisation anisotropy is a measure of how a γ ray has Compton scattered within a clover, either horizontally or vertically, after it initially struck the clover detector. The

intensity of the Compton scattered radiation depends on the direction of the electric field of the incident radiation. By observing the intensity of the scattered radiation at different positions about the scatter this will allow us, in most cases, to determine the direction of the electric field and therefore whether the radiation is magnetic or electric in character [9].

Polarisation anisotropy P is defined by

$$P = \frac{A}{Q}$$

where A is the experimental asymmetry between the vertically and horizontally scattered γ rays given by

$$A = \frac{N_V - \varepsilon N_H}{N_V + \varepsilon N_H}$$

N_V represents the number of vertical scatters of a γ ray while N_H represents the number of horizontal scatters of that γ ray. ε is an efficiency parameter determined by unpolarised γ rays from a ^{152}Eu source, and is required in the measurement of A as vertical and horizontal detectors could have different efficiency. $\varepsilon = N_V/N_H$ was determined to be ε =1.04 as an average of all γ rays detected in all detectors from an Eu source and ε was also seen to have no energy dependence attributed to it. Polarisation measurements are taken only in clovers at 90^o as this is where Q, the polarisation sensitivity is maximal and in tern the sensitivity of A will be maximal, resulting in the best results for P, the polarisation anisotropy. Polarisation sensitivity, Q, for clover detectors is determined by

$$Q = Q_0[0.31(2) + 7(2) \times 10^{-5} E_\gamma]$$

where E_γ is the energy of the transition measured in keV, and Q_0 is the polarisation sensitivity for an ideal polarimeter given by

$$Q_0 = \frac{(1+\alpha)}{(1+\alpha+\alpha^2)}$$

with α=E_γ[keV]/511 [17]. If the value of P is positive, the transition can be predicted to

be pure stretched electric in nature and if the value of P is negative the transition can be expected to be a pure stretched magnetic transition. However, for unstretched transitions the opposite can be expected to occur. Therefore, pure electric transitions would have a negative value of P while pure magnetic transition would be positive. In the case of mixed transitions, the value of P can vary from positive to negative and so the measured value of P must be compared to theoretical predictions. Theoretical predictions were carried out using the code "polar" and are calculated as a function of the mixing ratio, δ. δ is a ratio of the M1/E2 mixing of a transition, with pure dipole transitions having $\delta = 0$ [9]. For a $\Delta I = 1$ transition the mixing ratio is defined by

$$\delta^2 = \frac{I_\gamma(\lambda = 2)}{I_\gamma(\lambda = 1)}$$

where $I_\gamma(\lambda = 2)$ is the intensity of the quadrupole transition and $I_\gamma(\lambda = 1)$ is the intensity a dipole transition.

Chapter 2. Experiment

Experimental Setup

The experimental setup used in this experiment consisted of the AFRODITE array [1] at iThemba Laboratory for Accelerator Based Sciences (iThemba LABS). The apparatus also included neutron detection set up as a bank of 12 100 x 600 mm plastic scintillators placed in a double layer 1.93 m downstream of the target at $\theta = 0^\circ$ to the beamline as shown in Figure 8. The AFRODITE array, much like the EXOGAM array, has a rhombicuboctahedron shape, which can accommodate a maximum of 16 detectors with two opposing faces at 0° and 180° free to accommodate the beam pipe.

The target used was high purity ^{114}Cd with a thickness of ∼3 mg/cm^2. The beam consisted of a 25 MeV ^{3}He beam pulsed with 1/5 pulse selection with beam intensities ranging from 1 to 20 pnA. A 25MeV beam was used as this energy would allow us do distinguish between statistical neutrons of a few MeV and neutrons produced in the transfer. The beam was focused to a 3 mm spot size at the target.

Count rates in the clover detectors were limited to 10 kHz in order to achieve the best signal-to-noise ratio.

The primary reaction that occurred in the experiment was $^{114}_{48}\mathrm{Cd}_{66}(^3\mathrm{He},3\mathrm{n})^{114}_{50}\mathrm{Sn}_{64}$ with a relative yield of 86.1(5)%. Several other nuclei were populated in the reaction along with ^{114}Sn. The next most abundant nucleus was ^{114}In with a relative yield of 10.4(2)%. For the ^{115}In nucleus we calculated a relative yield of 3.02(8)% and the least abundant nucleus was ^{115}Cd and was found to have a relative yield of just 0.41(1)%. The relative yields of each nucleus were calculated by comparing the number of transitions to the ground state of each nucleus present in the data.

[1] AFRODITE is an acronym for AFRican Omnipurpose Detector for Innovative Techniques and Experiments

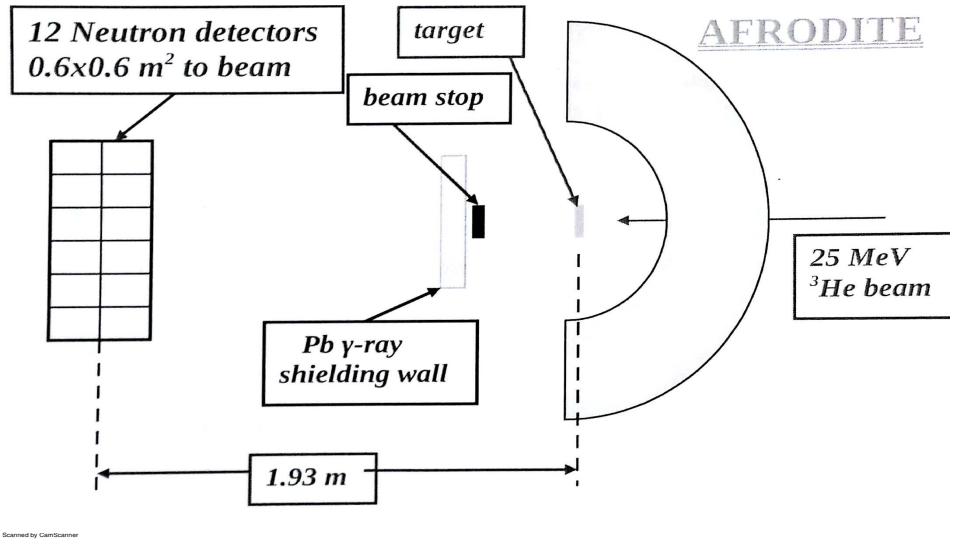

Figure 8: Schematic set-up for the ^{114}Cd(^{3}He,3n)^{114}Sn experiment [11].

The AFRODITE array in our experiment consisted of 9 high-purity germanium clover detectors (HPGe detectors). Each clover detector is made up of four separate n-type coaxial 50 x 70 mm HPGe crystals. Detectors 1 to 4 were placed at 135° to the beam line while detectors 5 to 9 were placed at 90° to the beamline. Figure 9 shows a photograph of the experimental setup used, with the 90° and 135° detector rings visible. The 9 HPGe detectors used in our experiment were given bismuth-germanate (BGO) anti-Compton shielding and had copper and aluminium absorbers attached to the front of the detector.

Figure 10 shows a schematic of the clover detectors used in the experiment. Clover detectors are advantageous as they can act as a polarimeter due to the detector having four different crystals, allowing polarisation measurements of γ rays to be taken. They are also less sensitive to neutron damage than other detectors such as Ge(Li) detectors. They are also more efficient when run in addback mode than detectors that are not used in addback mode. In addback mode, if a γ ray that is incident on a crystal in a detector and Compton scatters into an adjacent crystal in the same clover detector, the partial $\gamma-$ray energy deposited in first crystal during the first scattering event and the partial $\gamma-$ray energy deposited in the second crystal during the second scattering event are added together to reconstruct the total

energy of the γ ray that was emitted from the nucleus.

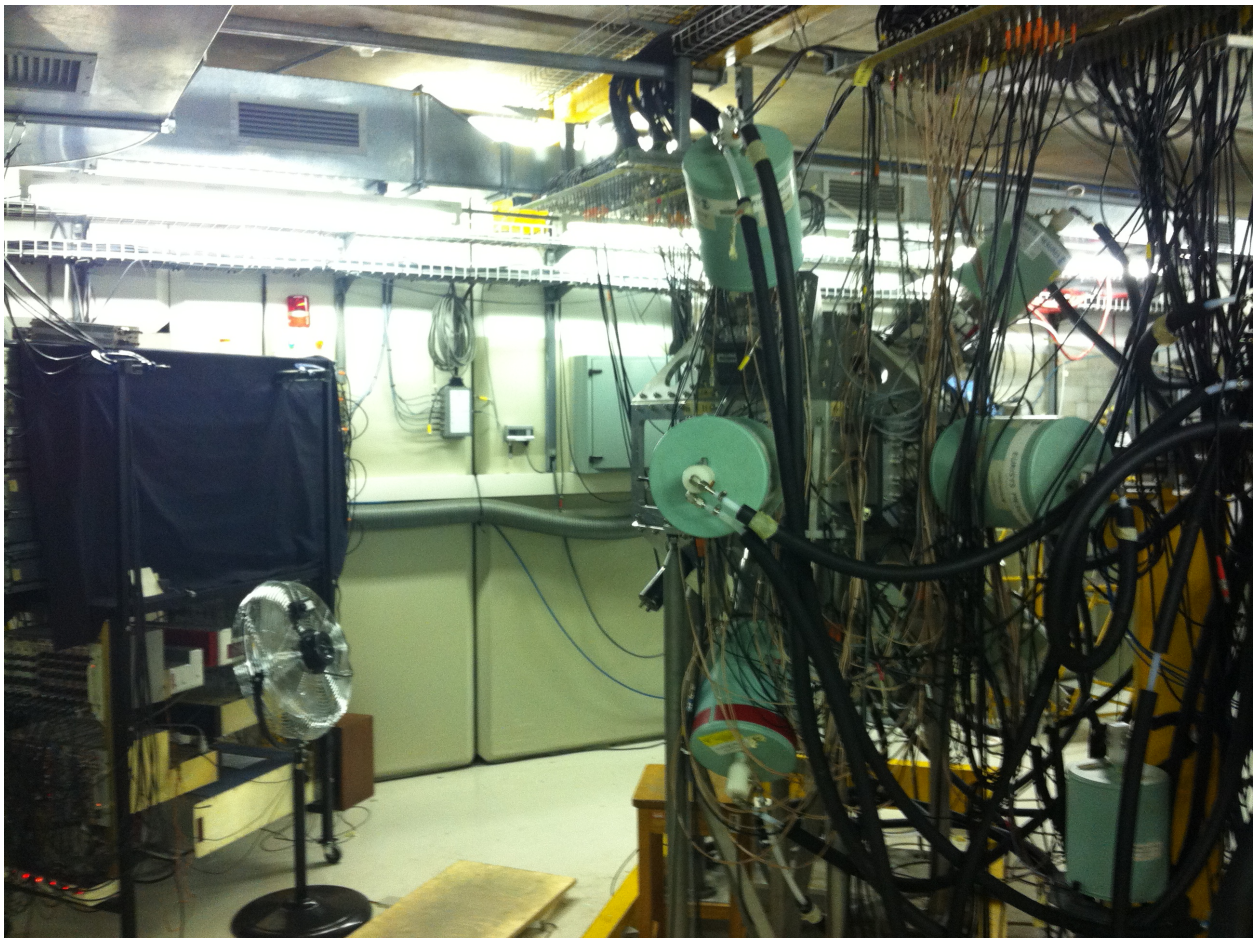

Figure 9: AFRODITE array setup used in this experiment. The beam enters the array from the right hand side of the image. The image shows the clover detectors in the $\theta = 90°$ ring and the $\theta = 135°$ ring about the beam line and also the bank of neutron detectors placed 1.93 m downstream of the array at $\theta = 0°$ about the beamline.

For efficient operation, the detectors are cooled to -180°C by an automated liquid nitrogen cooling system. The detectors are cooled by a 2.5 l liquid nitrogen dewar, and the sensitive HPGe crystals are continuously cooled by a copper rod connected to the liquid nitrogen dewar. The detectors are filled with liquid nitrogen from a 180 l liquid nitrogen supply tank and the level of liquid nitrogen in each detector is monitored and controlled by a programmable logic controller. Detector temperatures are monitored by an electronic alarm system connected to a dedicated PC which gives a readout of the detector temperatures along with a temperature history for each individual detector. The cooling system maintains the low temperature and is also used to monitor the temperature of individual detectors.

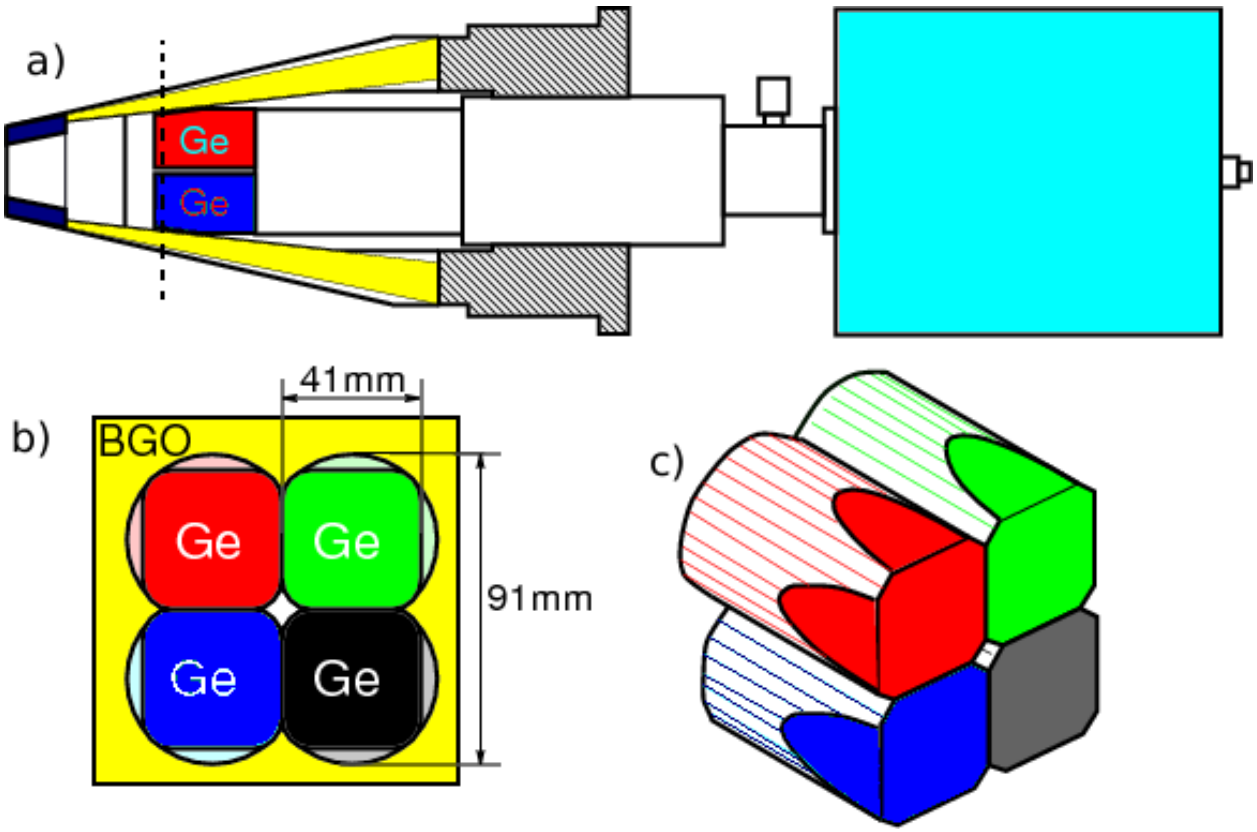

Figure 10: Schematic of the clover detectors used in the AFRODITE array. Image a) shows the entire clover detector with the BGO anti-compton shielding shown in yellow and on the right hand side is the liquid nitrogen dewar shown in pale blue. Image b) shows a cross section though the HPGe crystals of image a) along the dotted line. Image c) is a 3D representation of the HPGe crystals in their four-leaf clover arrangement.

The experiment was set up without any trigger conditions, therefore the data were written in singles mode, where all the decays were recorded with a timestamp. By recording the data in this way events can be chosen in the sorting after the experiment has finished. All the data were collected and recorded by software called Multi Instance Data Acquisition System (MIDAS) [15]. With the experiment set up in this way and being run for 46 hours, approximately 1.5 billion γ rays were recorded.

Count rates in the clover detectors were limited to 10 kHz in order to achieve the best signal-to-noise ratio.

After data collection had been completed the raw data were calibrated using ^{133}Ba and ^{152}Eu sources. Doppler shift correction was not required as the thickness of the target means that the product nucleus will have negligible velocity. The data was sorted into 4 $\gamma - \gamma$

matrices compatible with Radware [16]. The first matrix was a symmetric matrix which is used to build the level scheme containing clover-clover coincidences. The second matrix was an asymmetric directional correlation (DCO) matrix containing coincidences between 90° clovers and 135° clovers. γ rays from the 90° clovers were placed on the y-axis of the matrix while γ rays from the 135° clovers were placed on the x-axis of the DCO matrix. The third and fourth matrices were asymmetric matrices containing only γ rays detected in the 90° clovers on the y-axis of the matrix, against γ rays detected in all the clovers, placed on the x-axis of the same matrix. The third matrix is comprised of only γ rays that had undergone horizontal scattering between the elements of the 90° clovers, while the fourth matrix contained only γ rays that had undergone vertical scattering between the elements of the 90° clovers. A vertical scatter is one where the γ ray scatters between elements perpendicular to the direction of the beamline, while a horizontal scatter is one where the γ ray scatters parallel to the direction of the beamline. These last 2 matrices were used in the polarisation analysis of the data. The DCO matrix and the polarisation matrices were used in conjunction to assign spin and parity to the nuclear states found in the level scheme.

Chapter 3. Results

Level Scheme

The ^{114}Sn level scheme presented in this thesis contains 11 bands, although some of these are merely collections of γ rays labelled as bands for convenience. The new level scheme also contains six new γ rays, listed in Table 1 and we have relocated the position of one γ ray that was in a previous level scheme [19] to a new position.

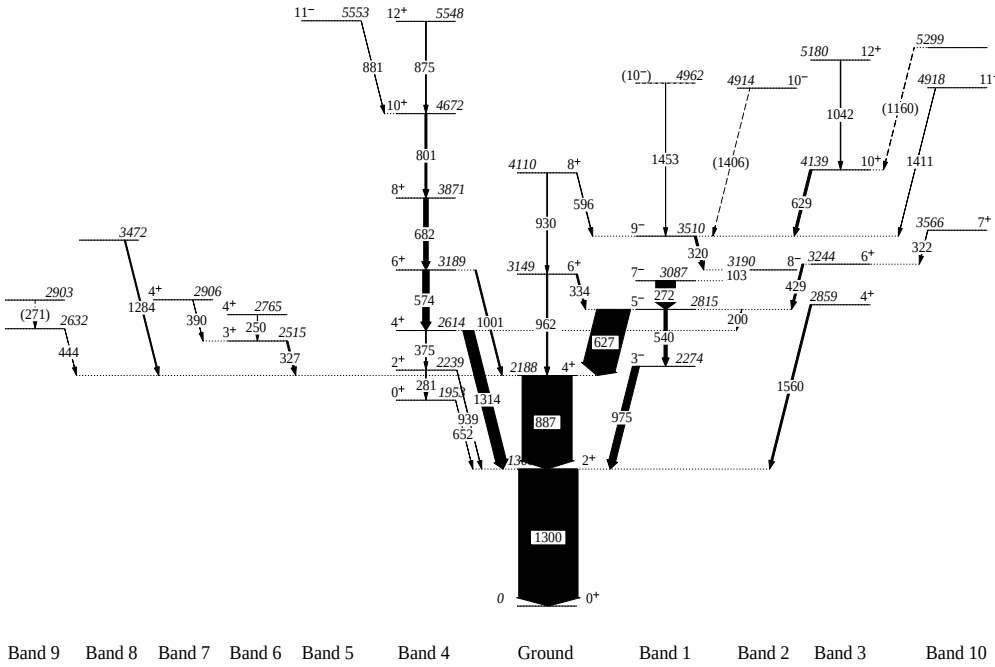

Figure 11: Level scheme of ^{114}Sn. Arrow widths are proportional to γ ray intensity and all energies are in keV.

Figure 11 shows the full level scheme of ^{114}Sn, and includes all the newly added bands, Bands 8 and 9, and new γ rays that were added to existing bands.

Table 1 shows the energy of the new γ rays, the initial and final bands that the decay is from and to, as well as the initial and final spin and energy states of each decay.

E_γ(keV)	Initial Band	Final Band	Initial E(keV)	Final E(keV)	Initial I^π	Final I^π
271	9	9	2903	2632		
322	10	3	3566	3244	7^+	6^+
429	3	2	3244	2815	6^+	5^-
444	9	Ground	2632	2188		4^+
1160	10	3	5299	4139		10^+
1284	8	Ground	3472	2189		4^+

Table 1: Table of new decays in level scheme, shown in order of ascending energy of the γ ray.

Positions of the new γ rays

In this section is a discussion of the newly added bands in Figure 11, and the reasoning behind the positioning of each new γ ray in the level scheme. The bands will discussed in order from left to right across the level scheme, therefore starting at Band 9 then moving on to Band 8 followed by Band 3 and finally end off with the levels in Band 10.

Starting at Band 9. This band contains 2 states at 2632 keV and at 2903 keV. The 2632-keV level decays via a new 444-keV γ ray to the 2188-keV, 4^+ state of the ground state band. The 444-keV γ ray was found to be in coincidence with the 887-keV and the 1300-keV γ rays located in the ground state band, while it was not in coincidence with the 627-keV γ ray which feeds the 4^+ level of the ground state band from the side. This is shown in Figure 12, which shows the coincidence spectrum when a gate is set on the 444-keV γ ray as well as the coincidence spectrum when a gate is set on the 261-keV γ ray. In the spectrum gated on 444 keV, peaks can be seen at 887 keV and 1300 keV but no peak at 627 keV is visible.

The peak seen at 261 keV, in the spectrum gated on 444 keV, is attributed to a coincidence between a 444-keV γ ray and a 261-keV γ ray in ^{115}In which is another residual nucleus seen in the data. Figure 13 shows the level scheme of ^{115}In.

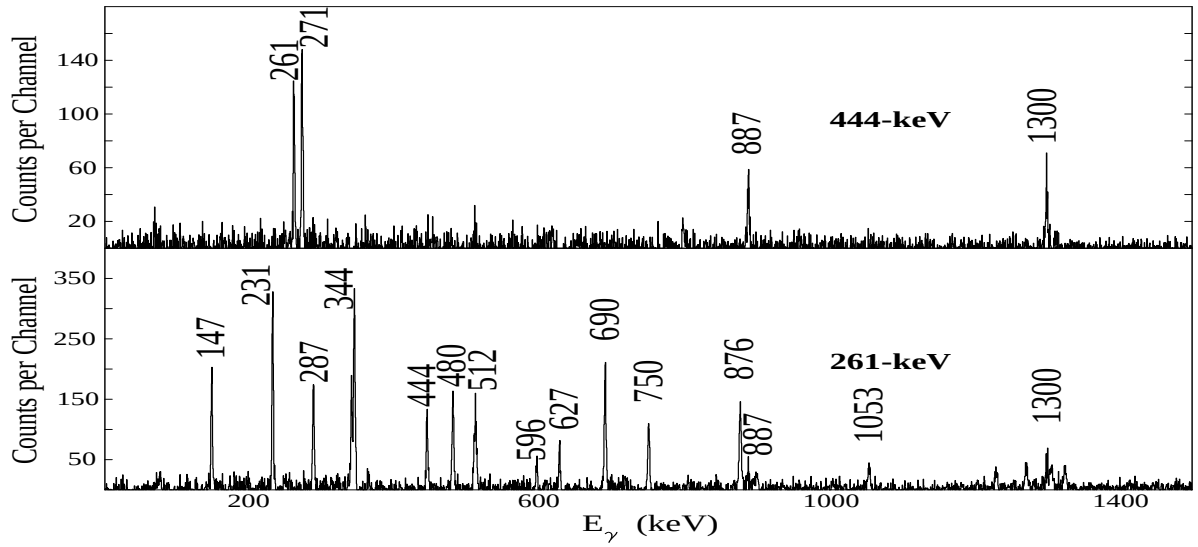

Figure 12: Coincidence spectrum gated on the 444-keV γ ray in the top panel along with the coincidence spectrum gated on the 261-keV γ ray in the bottom panel.

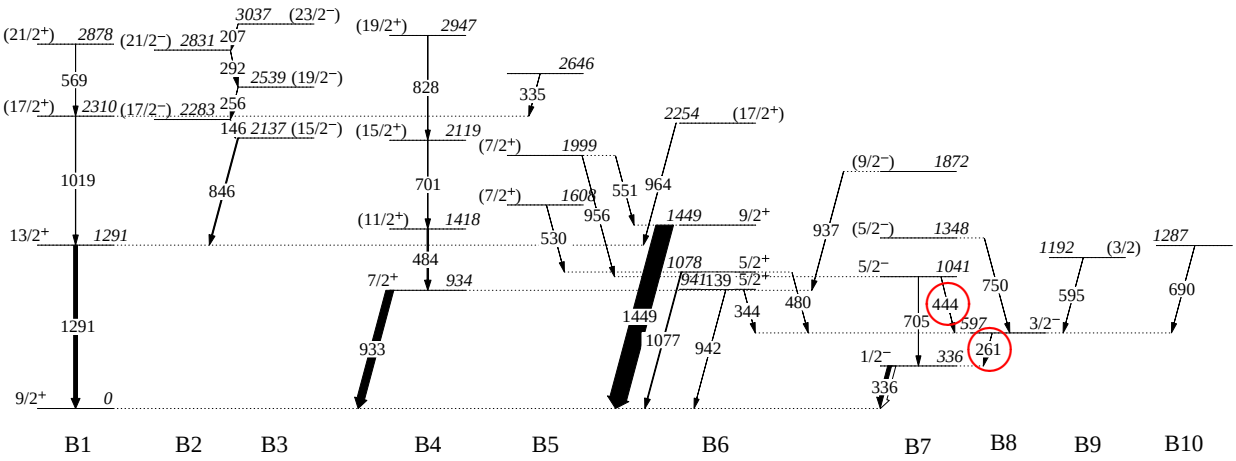

Figure 13: Level scheme showing the levels present in ^{115}In [16] seen in the data. The red circles highlight the 444-keV γ ray and a 261-keV γ ray in the level scheme.

This coincidence between the 444-keV γ ray and a 261-keV γ ray raises the question: is the 444-keV γ ray in ^{114}Sn or ^{115}In? Figure 13 shows the level scheme of ^{115}In and the coincidence spectrum when a gate is placed on the 261-keV γ ray can be seen in the bottom panel of Figure 12. Figure 13 shows a 336-keV γ ray in coincidence with the 261-keV γ ray, however a 336-keV γ ray cannot be seen in the bottom panel of Figure 12. The 336-keV γ

ray cannot be seen because it is de-exciting a state that has a half-life of approximately 4.5 hours [2], therefore this γ ray may only occur after the event window has closed and will not be shown in the coincidence spectrum.

When we place a gate on the 261-keV γ ray we see contaminant peaks at 887 keV and 1300 keV which are present in ^{114}Sn, therefore if we gate on the 444-keV transition we are likely to see contamination from transitions in ^{114}Sn even if a 444-keV transition is not present in ^{114}Sn. This makes it difficult to decide if the 444-keV γ ray is in ^{114}Sn or ^{115}In. However we are able to resolve the question in the following manner. We first place a gate on the 261-keV $\gamma-$ ray in ^{115}In and then calculate the ratio of the area of the 887-keV peak to the area of the 444-keV peak. We then place a gate on the 444-keV γ ray and calculate the ratio of the area of the 887-keV peak to the area of the 261-keV peak. If the ratio is larger when the gate is placed on the 444-keV γ ray then that must mean that the 444-keV γ ray is in fact part of the ^{114}Sn level scheme. When we place a gate on the 261-keV γ ray we find that the ratio of $A(887)/A(444)$ is 0.21(1) where $A(887)$ represents the area of the 887-keV peak in the gated spectrum, and when we place the gate on the 444-keV $\gamma-$ ray the ratio of $A(887)/A(261)$ is 1.24(6). We can therefore conclude that the 444-keV γ ray is indeed part of the ^{114}Sn decay scheme and that the 2632-keV level is seen in the ^{114}Sn nucleus.

Now that we have established that the 2632-keV level is present in Band 9 we can turn our attention to the 271-keV γ ray which feeds this level. Placing the 271-keV γ ray was difficult because of the presence of a very intense 272-keV decay found in Band 1. For example when we set a gate on the 271-keV γ ray we also, unavoidably, set a gate on the 272-keV γ ray, and because of its high intensity we are then unable to see any γ rays that may be in coincidence with the weaker 271-keV transition alone. The 271-keV γ ray in Band 9 was placed above the 444-keV γ ray due to its coincidence with the 444-keV γ ray in the same band as seen in Figure 12. When a gate is placed on the 444-keV transition we should not see any coincidence with the 272-keV transition in Band 1. But there is clearly a coincidence between the 444-keV transition and the 271-keV transition, seen in Figure 12. There is no 271-keV γ ray in ^{115}In and for this reason we believe there is a 444-keV transition

in coincidence with a 271-keV transition in ^{114}Sn.

We turn our attention now to Band 8. This band contains a single state at 3472 keV, which decays via a 1284-keV γ ray to the 2188-keV, 4^+ state in the ground state band. The 1284-keV γ ray and consequently also the level at 3472 keV are both new additions to the level scheme. When a gate is set at 1284 keV, as shown in Figure 14, strong peaks are observed at 887 keV and 1300 keV, which are transitions in the ground state band itself, depopulating the 4^+ and 2^+ states respectively. It is therefore most likely that the 1284-keV γ ray directly populates the 2188-keV, 4^+ state in the ground state band. This conclusion is consistent with the fact that no 627-keV γ ray is seen when a gate is set on the 1284-keV transition. The 627-keV γ ray also feeds the 4^+, 2188-keV state in the ground state band and it must therefore decay parallel to the 1284-keV γ ray.

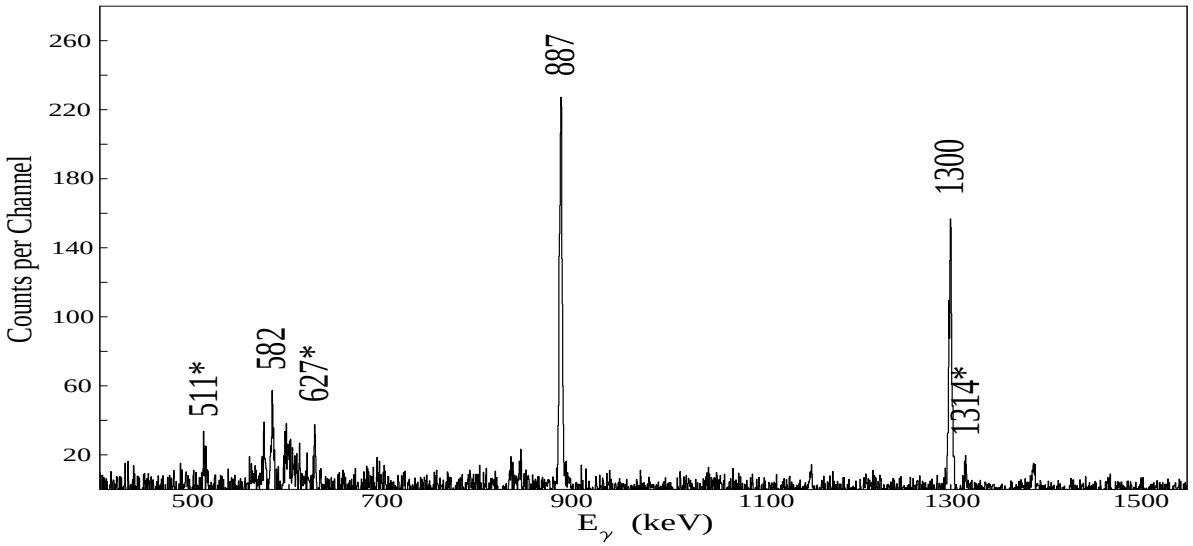

Figure 14: Spectrum gated on the 1284-keV γ ray. γ rays labelled with an asterisk (*) are significant contaminants in the spectrum. The 511-keV peak is attributed to electron-positron annihilation.

In Figure 14 a peak is also visible at 582 keV but this is due to a coincidence between the 1284-keV and the 582-keV γ ray in ^{113}Sn.

We now focus our attention on Band 3. In a previous level scheme of ^{114}Sn, a γ ray of 429 keV was placed in such a way that it decayed into the 3088-keV, 7^- state of Band 1 [18].

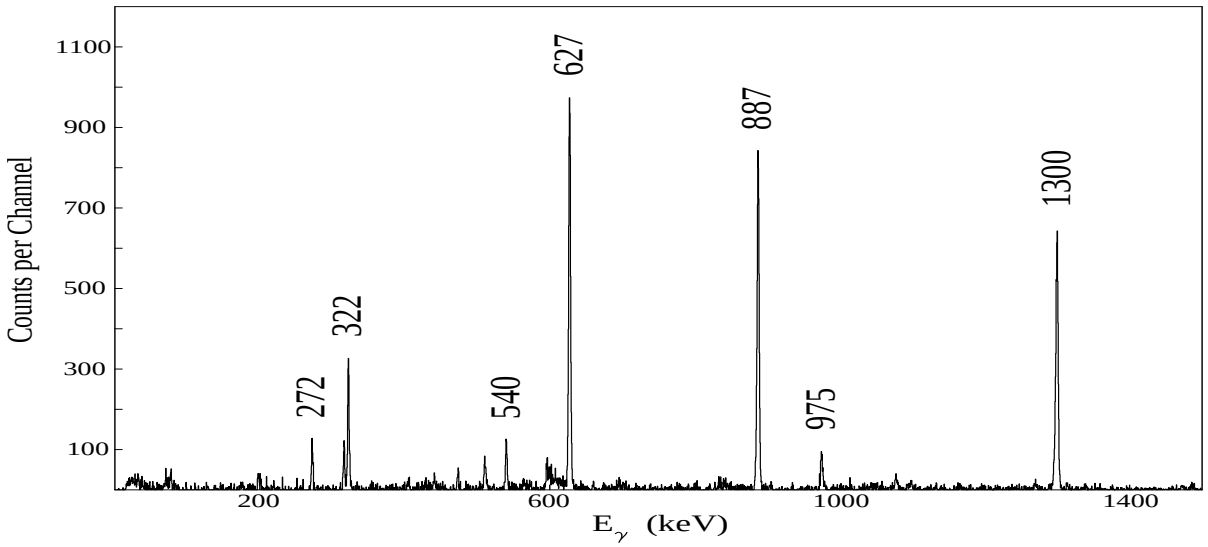

Figure 15: Coincidence spectrum gated on the 429-keV γ ray.

The presence of a peak at 272 keV when a gate is set at 429 keV (see Figure 15) suggests that the 429-keV γ ray might in fact decay into the 7^- state of Band 1 as seen in older decay schemes. If a gate is set on any transition that feeds the 7^- state we expect to see the same ratio of $A(272)/A(627)$, but if we gate on the 103-keV transition, which is known to populate the 7^- state, the ratio of intensities of the 272-keV γ ray to the 627-keV γ ray is much larger than when a gate is placed at 429 keV. When we look at the ratio of $A(272)/A(627)$ with a gate set on the 103-keV transition we obtain a value of 0.95(1). When we calculate the same ratio but with the gate set on the 429-keV transition instead, the ratio is found to be 0.11(1). If the 429-keV γ ray was indeed feeding the 7^- state, and was therefore parallel to the 103-keV γ ray, as claimed in earlier decay schemes, then the ratio of intensities of the 272-keV peak to the 627-keV peak would have to be the same in both the 103-keV and the 429-keV gates. What we find is that the ratio is much lower when the gate is set on the 429-keV transition compared to when the gate is set on the 103-keV transition. This difference in the ratio suggests that the 103-keV γ ray and the 429-keV γ ray are not parallel and therefore that the 429-keV γ ray does not populate the 7^-, 3088-keV level in Band 1. Our data suggests that in fact the 429-keV γ ray actually decays into the 2815-keV, 5^- level of Band 1 instead of the 7^- state. Therefore we have added a new 3244-keV level to Band 3, which decays via the 429-keV γ ray. The spin and parity assignment (6^+) of this level is

discussed at a later stage. Figure 15 shows the coincidence spectrum observed by gating on 429-keV γ ray. In this spectrum peaks for 627 keV, 887 keV and 1300 keV can clearly be seen, as well as smaller peaks of 540 keV, 975 keV. All these peaks suggest that the 429-keV γ ray populates the 5^-, 2815-keV level of Band 1.

We also find that when a gate is set on the 272-keV γ ray there is no peak present at 429 keV as seen in Figure 16. This evidence suggests that there is no coincidence between the 429-keV and 272-keV γ rays in ^{114}Sn. The 272-keV peak seen in Figure 15 may be attributed to another 272-keV γ ray that has yet to placed in the level scheme.

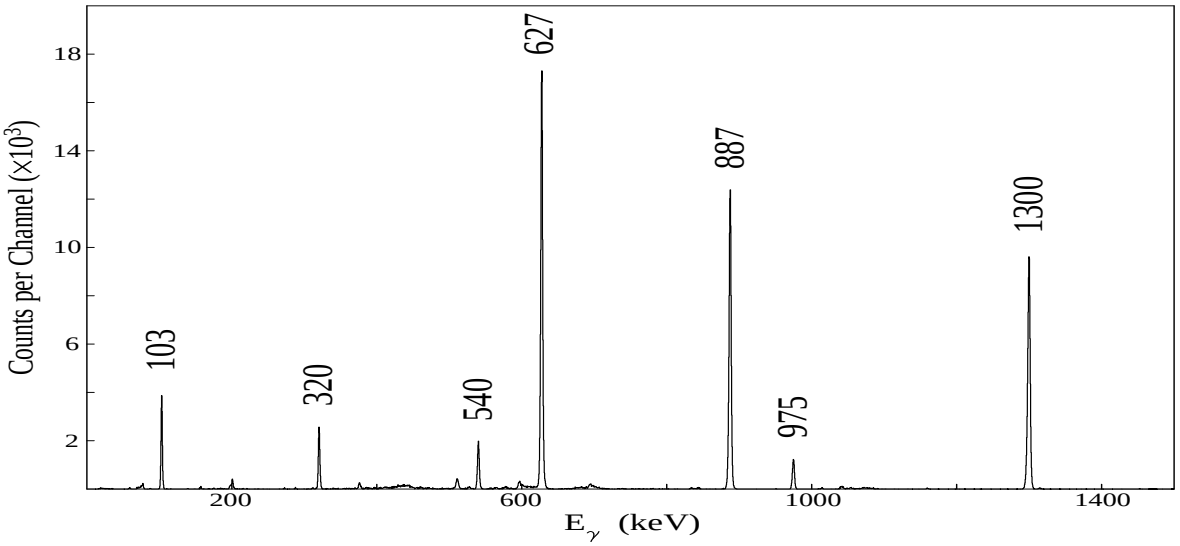

Figure 16: Coincidence spectrum gated on 272-keV γ ray.

We now look at Band 10 in ^{114}Sn, where we have added a new level at 3566 keV. This level decays via a 322-keV γ ray into the 3244-keV, 6^- state of Band 3. When a gate is placed on the 429-keV γ ray, that depopulates that state, a peak is present at 322 keV, as seen in Figure 15. When we gate on the 322-keV transition we get the spectrum shown in Figure 17, which shows a peak at 429 keV. However this is a "dirty" gate as there is a very strong 320-keV transition present in the level scheme. This means that we need to be sure that the peak at 429 keV in Figure 17 is not due to inadvertently setting a gate on the 320-keV γ ray. When we do gate on the 320-keV transition, Figure 18, we find that there is no 429-keV transition in the spectrum. We made sure that the gate set at 320 keV was

a "clean" gate by gating at an energy slightly lower than 320 keV therefore ensuring that we would not see any transitions that may be in coincidence with the 322-keV γ ray. These pieces of evidence have led to the conclusion that there is a new 322-keV transition feeding the 3244-keV state in Band 3 in ^{114}Sn.

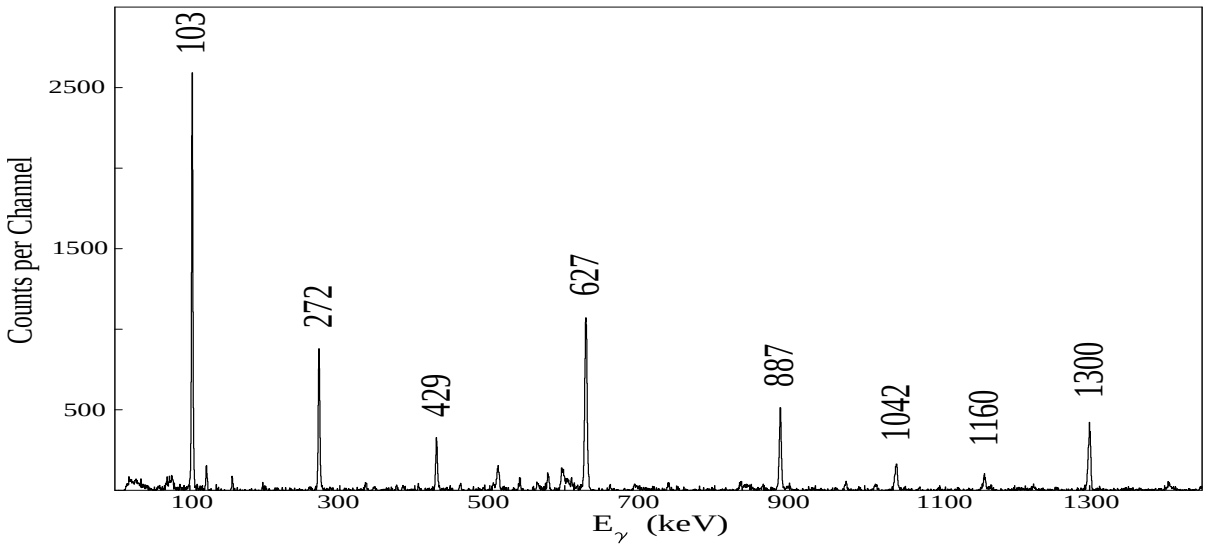

Figure 17: Coincidence spectrum gated on the 322-keV γ ray.

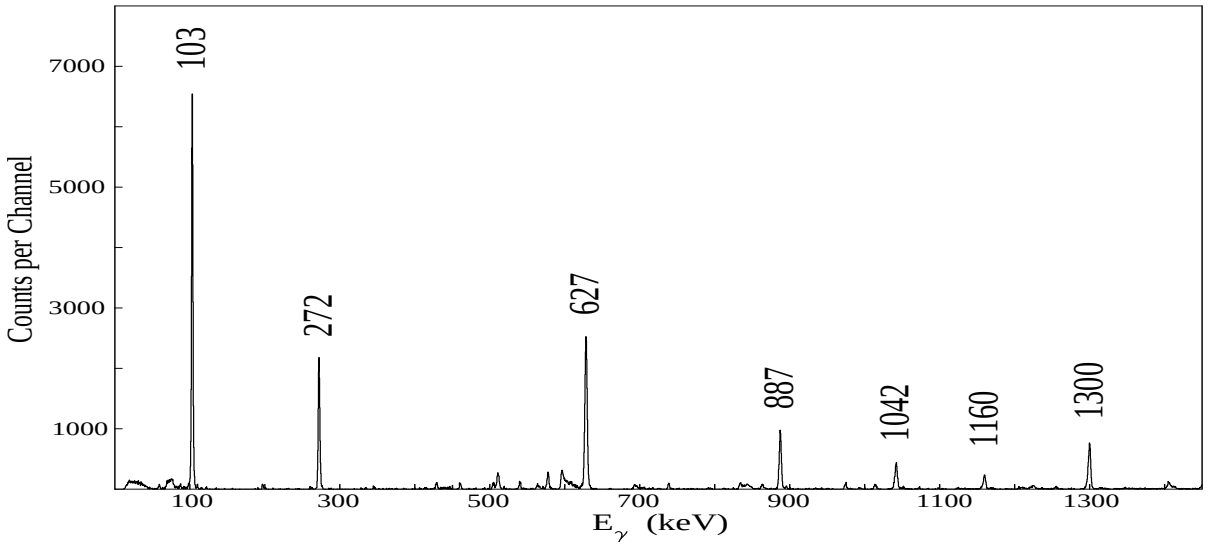

Figure 18: Coincidence spectrum gated on the the 320-keV γ ray.

Continuing to focus on Band 10, there is also a new 12^+, 5299-keV level that has been added. An 1160-keV γ ray depopulates this level and feeds into the 10^+, 4139-keV level in

Band 3. This 1160-keV decay was placed in its present position based on its coincidence spectrum shown in Figure 19.

In Figure 19 peaks can be seen for all the most intense transitions in the decay scheme shown in Figure 11, and we can see peaks for each γ ray in the decay pathway of the 5299-keV level to the ground state of ^{114}Sn. The peak at 574 keV suggests that the 1160-keV γ ray may also directly populate Band 4, where a strong 574-keV transition can be found. We were unable to find any specific links between the 10^+ state fed by the 1160-keV transition and Band 4, and therefore cannot draw any conclusions as to where this link occurs.

There could be two possible missing links from the 9^- state in Band 1 to the 6^+ state in the ground state band and from the 9^- state in Band 1 to the 6^+ state in Band 4 may account for the 334-keV and 574-keV peaks seen in Figure 19. The peak at 334 keV may be associated with a coincidence between the 1160-keV γ ray and the 334-keV γ ray that decays from the 6^+, 3149-keV level in the ground state band into the 5^-, 2814-keV level in Band 1. This coincidence suggests that there could be link between the 10^+ state fed by 1160-keV γ ray and the 6^+ state in the ground state band, but no specific link could be seen in the data. The peak at 574 keV may be associated with a coincidence between the 1160-keV γ ray and the 574-keV γ ray that decays from the 6^+, 3189-keV level in Band 4 into the 4^+, 2614-keV level in Band 4. This coincidence suggests that there could be link between the 10^+ fed by 1160-keV γ ray and the 6^+ state in the Band 4, but again no specific link could be seen in the data.

If we gate on the 1160-keV transition, we expect to see a peak at 272 keV. We also expect to see that the intensity of the peak at 272 keV is approximately the same as the intensity of the peak seen at 103 keV in the same 1160-keV gate. This however is not the case as the intensity of the 272-keV peak is much smaller than the intensity of the 103-keV peak. One possible explanation for this lower-than-expected intensity may be that perhaps there are several low-intensity transitions out of the 7^- state, parallel to the 272-keV transition. This could provide alternative decay paths and thus reduce the intensity of the 272-keV

peak. The low intensity of the 272-keV transition in the gated spectrum led us to place the 1160-keV γ ray tentatively in its present position, decaying out of Band 10. This tentative position is the best possible position for the 1160-keV γ ray, even though it may possibly be in conflict with the low intensity of the 272-keV transition.

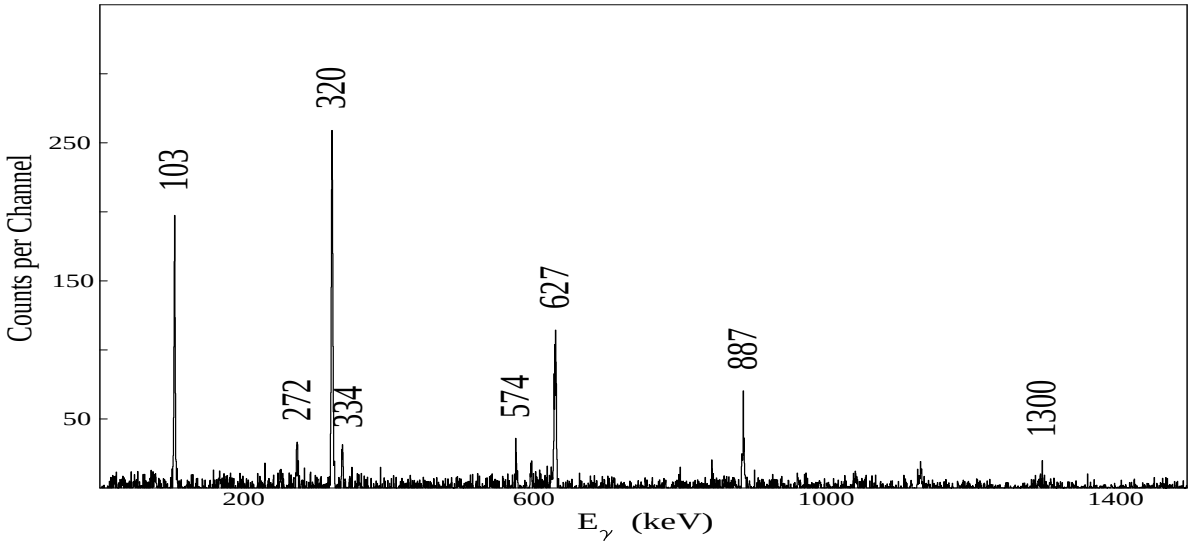

Figure 19: Coincidence spectrum gated on the 1160-keV γ ray.

We have now discussed the positioning of all the newly added levels and decays seen in the data set.

Spin and Parity

Spin and parity allocations were made using DCO ratio analysis and polarisation anisotropy analysis (referred to as PDCO analysis). The PDCO analysis generally allows the multipolarity of γ rays to be determined. In this way we will be able to assign the spin and parity of most of the new levels in Figure 11. If we have a level with known spin and parity, and are able to determine the multipolarity of the γ ray that populates that level, we can then determine the unknown spin and parity of the state that is depopulated by that transition. DCO and polarisation values were calculated for all the transitions in the level scheme and shown in Tables 2 and 3 respectively. Benchmark DCO values were calculated by taking an average of the DCO values of some E1 and E2 transitions in our data that are previously

known to be in ^{114}Sn. Pure E1 transitions were found to have a benchmark DCO value of 0.88(9) while pure E2 transitions had a DCO value of 1.07(4). We will start by looking at the levels in the new bands in the level scheme and then move on to the new levels that are in previously existing bands. We will discuss the bands in the same order as in the previous section therefore we will move from left to right across the level scheme. DCO ratio and Polarisation values for the new transitions in the levels scheme have been extracted from Tables 2 and 3 and placed in Tables 4 and 5 respectively.

Gate (keV)	E_γ(keV)	R_{DCO}	error
1300	334	0.78	(0.03)
1300	627	1.00	(0.01)
1300	887	1.02	(0.01)
1300	939	0.99	(0.12)
1300	975	0.88	(0.02)
1300	1314	1.04	(0.02)
1300	1560	1.19	(0.07)
272	103	0.85	(0.01)
272	200	0.90	(0.06)
272	320	0.86	(0.02)
272	540	1.06	(0.02)
272	975	0.99	(0.02)
272	1042	1.07	(0.14)
272	1160	1.02	(0.26)
272	1406	0.92	(0.21)
272	1453	1.04	(0.17)
962	887	1.15	(0.03)
962	1300	1.14	(0.03)
887	271		
887	272	1.02	(0.01)
887	322	0.69	(0.14)
887	327	0.85	(0.03)
887	390	0.69	(0.45)
887	429	0.82	(0.03)
887	444		
887	596	0.80	(0.03)
887	962	1.11	(0.06)
887	1001	1.07	(0.07)
887	1284	1.09	(0.09)
682	375	0.64	(0.15)
682	574	1.08	(0.02)
682	801	1.01	(0.03)
682	875	1.08	(0.09)
801	682	1.09	(0.03)
801	881	0.95	(0.71)
327	250	1.14	(0.19)
327	390	1.10	(0.13)

Table 2: Table of DCO ratio values and errors for all transitions in the level scheme, grouped by the gating transition used to determine the DCO ratio.

Gate (keV)	Transition (keV)	A	ΔA	Q	P(%)	ΔP(%)
320	596	5.9	(7.8)	0.22	27	(36)
320	1453	-12	(13)	0.13	-87	(100)
320	1406	-52	(41)	0.14	-385	(310)
320	1160	-3	(28)	0.15	-22	(190)
320	629	-6.4	(3.4)	0.21	-30	(17)
320	1042	-4	(13)	0.16	-24	(80)
320	1411	9	(29)	0.14	69	(220)
327	390	13	(26)	0.25	50	(100)
327	250	45	(47)	0.28	160	(170)
887	327	2.7	(2.7)	0.27	10	(10)
887	1284	5.1	(7.8)	0.14	36	(55)
887	444	-12	(21)	0.24	-50	(88)
887	962	5.0	(5.1)	0.17	29	(30)
887	1001	17.7	(6.7)	0.17	107	(42)
887	627	2.20	(0.50)	0.21	10	(2.5)
887	1300	3.30	(0.60)	0.14	23	(5.2)
272	103	6.8	(3.1)	0.31	22	(10)
272	320	-2	(72)	0.27	-7	(270)
272	200	-31	(21)	0.29	-106	(71)
272	540	-2	(64)	0.23	-8	(280)
627	429	11.4	(3.4)	0.25	46	(14)
627	322	6	(21)	0.27	24	(80)
627	334	-3	(10)	0.26	-10	(40)
627	272	1.00	(0.30)	0.28	3.8	(1.1)
962	930	-6	(48)	0.17	-35	(280)
1300	887	1.60	(0.40)	0.18	8.9	(2.5)
1300	975	8.3	(2.3)	0.17	49	(15)
1300	1560	13.9	(7.7)	0.13	109	(63)
1300	652	-13	(34)	0.21	-61	(160)
1300	939	11	(12)	0.17	66	(71)
1300	1314	9.4	(2.0)	0.14	67	(17)
375	281	-41	(38)	0.28	-147	(140)
375	574	30	(14)	0.22	135	(63)
801	682	9.7	(3.4)	0.20	48	(18)
801	875	5	(10)	0.18	27	(56)
801	881	-26	(37)	0.18	-147	(210)
681	375	-16	(30)	0.26	-64	(120)
681	801	11	(4.0)	0.19	58	(22)

Table 3: Table of polarisation anisotropy values and errors for all decays in the level scheme, grouped by the gating transition used to calculate the polarisation value for the specified γ ray. ΔQ=0.02 for all values Q.

Transition (keV)	DCO	error	Gate
271			887
322	1.35	(0.27)	627
429	0.82	(0.02)	887
444			887
1160	1.02	(0.26)	272
1284	1.09	(0.09)	887

Table 4: Extract from Table 2 showing DCO ratio values for the newly added decays in the level scheme, shown in order of ascending energy of the γ ray.

Transition (keV)	A	ΔA	P(%)	ΔP(%)	Q	ΔQ	Gate
271	3.6	(9.1)	13	(33)	0.28	(0.02)	444
322	6.4	(21)	24	(80)	0.27	(0.02)	627
429	11.0	(3.0)	46	(14)	0.25	(0.02)	627
444	-12	(21)	-50	(88)	0.24	(0.02)	887
1160	-3	(28)	-22	(190)	0.15	(0.02)	320
1284	5.1	(7.8)	36	(55)	0.14	(0.02)	887

Table 5: Extract from Table 3 showing the polarisation anisotropy values for newly added decays in the level scheme, shown in order of ascending energy of the γ ray.

We will begin by looking at Band 9. When calculating the DCO ratios, a gate must be set on a suitable E2 transition, but in the case of Band 9 there is no suitable gating E2 transition that allows for an accurate DCO ratio to be calculated. Polarisation anisotropy values however were obtained for the 271-keV and the 444-keV transitions, because it is not compulsory to gate on an E2 transition. However, using this method of gating, the results obtained have significantly large uncertainties due to low intensities and small peak areas. The 444-keV transition has a polarisation value of -50(88)% when a gate is set on the 887-keV decay. This polarisation value's sign couldn't be determined due to the large uncertainty associated with it and does not allow us to determine the multipolarity of the 444-keV γ ray.

When a gate is set on a 444-keV transition it is found that the 271-keV transition is very weak, it is also very close in energy to the intense 272-keV transition in Band 1 and therefore when setting a gate on 271-keV we also set a gate on the strong 272-keV transition, resulting in a polarisation value of 13(33)%. This polarisation value's sign also couldn't be determined therefore we cannot determine the nature of the 271-keV γ ray.

Spin and parity allocations for the states in Band 9 were thus not possible due to the low intensities of the 271-keV transition and the 444-keV transition, along with the fact that if a gate is set on a suitable E2 γ ray, such as the 887-keV γ ray, then the intensity of the 272-keV transition dominates the 271-keV transition by orders of magnitude.

We now turn out attention to Band 8, consisting of one new level which decays via a single 1284-keV γ ray to the ground state band. We were able to determine a DCO ratio for the 1284-keV transition of 1.09(9). This DCO value allows for the transition to be an E2 transition or a mixed M1/E2 transition. Figure 20 shows the measured DCO value plotted along with several calculated DCO values. However, in Figure 20 the measured DCO value intersects with both the curves for ΔI=0 and ΔI=1. We therefore cannot conclude whether the 1284-keV γ ray has a ΔI=0 or 1. The polarisation value for the 1284-keV transition was found to be 36(55)%. The positive polarisation value suggests a stretched electric or unstretched magnetic transition but unstretched electric or stretched magnetic transitions cannot be ruled out due to the large uncertainty of the polarisation value. Therefore these PDCO results suggest either a stretched E2 transition or a mixed M1/E2 transition. Neither stretched E2 transition nor mixed M1/E2 transitions involve a change of parity. Therefore we can conclude that the 3472-keV state will likely be of positive parity. However, we cannot draw any conclusion as to the spin of the state as the PDCO values allow for this state to be either 5^+ or 6^+.

Turning our attention to Band 3, the 429-keV γ ray that decays from Band 3 to Band 1 was found to have a DCO ratio of 0.82(3), which is consistent with a pure stretched dipole transition as when compared to our benchmark values. This DCO value suggests that this transition involves a spin change of ΔI=1. However this value does not rule out an unstretched dipole transition. Figure 21 shows the measured DCO ratio of the 429-keV γ ray plotted with two curves which depict calculated DCO ratios for two likely types of transition. The first curve, labelled 5-5-4-2, shows the DCO ratio in the case that the 429-keV γ ray might be a ΔI=0 transition. The label 5-5-4-2 means that the curve represents calculated DCO values for a dipole transition of $5 \rightarrow 5$ when a gate is set on a pure quadrupole 4

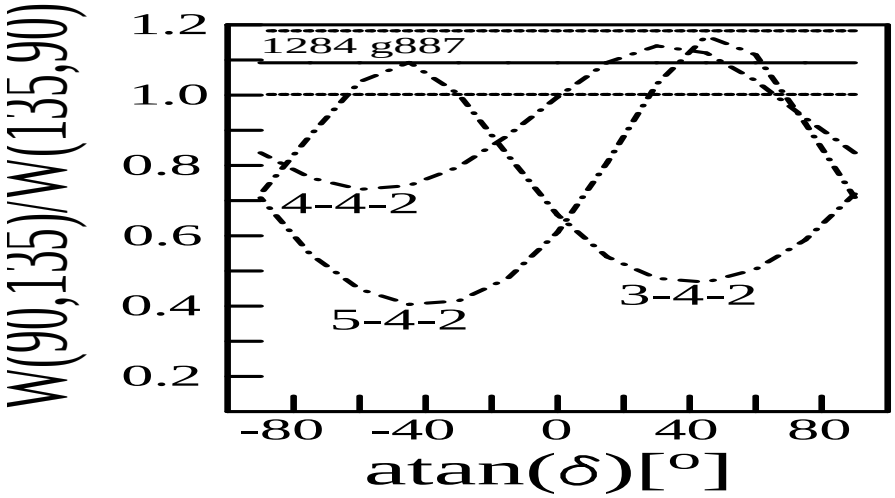

Figure 20: Measured value of R_{DCO} for the 1284-keV γ ray shown with error bars, plotted as a function of mixing ratio, δ. The curved broken lines are labelled with their corresponding spin sequence.

$\rightarrow$ 2 transition. The second curve, labelled 6-5-4-2, shows the DCO ratio in the case that the 429-keV γ ray might be a ΔI=1 transition. The label 6-5-4-2 means that the curve represents calculated DCO values for a dipole transition of 6 $\rightarrow$ 5 when a gate is set on a pure quadrupole 4 $\rightarrow$ 2 transition. When we examine Figure 21 we see that the horizontal line which represents the measured DCO value for the 429-keV transition intersects both curves. The intersection with the 5-5-4-2 curve allows for the 429-keV transition to be unstretched dipole but is unclear if the transition is magnetic or electric. However when we look at Weisskopf estimates for M1 and E1 transitions we see that E1 transitions are 40 times more likely to occur than M1 transitions for γ rays of this energy in ^{114}Sn. However, the likelihood of the 429-keV transition being an unstretched E1 transition is small as we would expect the polarisation value to be negative. The measured polarisation value is 46(14)% and this would rule out an unstretched E1 transition. Weisskopf estimates [12] can be calculated using the following equations,

$$\lambda(E1) = 1.0 \times 10^{14} A^{2/3} E^3$$

$$\lambda(M1) = 5.6 \times 10^{13} E^3$$

where λ is the inverse lifetime in s^{-1}, A is the atomic mass number and E is the energy of the transition in MeV.

The intersection with the 6-5-4-2 curve suggests that the 429-keV γ ray has ΔI=1. Further, the polarisation anisotropy value of 46(14)% is consistent with stretched electric or unstretched magnetic transitions. If the transition were unstretched E1 the polarisation value would be negative, while a stretched E1 transition would have a positive polarisation value. Therefore these PDCO values suggest that the 429-keV γ ray is a stretched E1 transition. Since 429-keV γ ray populates the 5^-, 2815-keV level in Band 1, and is a stretched E1 transition then the 3244-keV level in Band 3 that is being depopulated must have a spin and parity of 6^+.

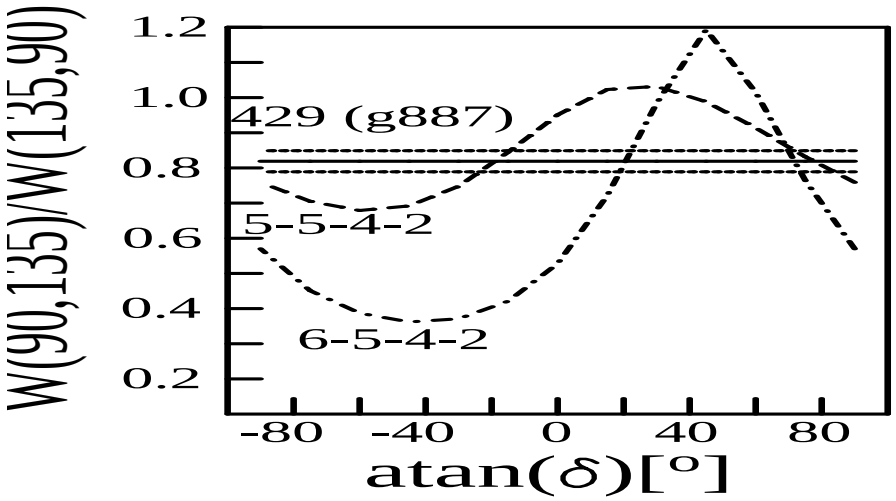

Figure 21: Measured value of R_{DCO} for the 429-keV γ ray shown with error bars, plotted as a function of mixing ratio, δ. The curved broken lines are labelled with their corresponding spin sequence.

We will now look at Band 10. The DCO ratio of the 1160-keV γ ray that feeds into the 10^+ state of Band 3 was found to be 1.02(26) when a gate is set on the 272-keV, $7^- \rightarrow 5^-$, transition. The 1160-keV decay also has a polarisation value of -22(185)%. These values result in no constraints as to what the multipolarity of the 1160-keV γ ray may be.

Therefore no spin or parity assignments can be made for this level as both the DCO ratio and the polarisation anisotropy for the transition must both be know for spin and parity assignments to be made accurately.

The 3566-keV level in Band 10 is depopulated by a 322-keV γ ray. The 322-keV γ ray has a DCO ratio of 0.70(14) and a polarisation anisotropy value of 24(80). These two values suggest that the 322-keV γ ray is a mixed M1/E2 with ΔI=1 transition decaying into 6^+ state of Band 3. This requires the 3566-keV level of Band 10 to have a spin and parity of 7^+.

At this point, we have discussed all the spin and parity assignments made for the new levels seen in the decay scheme.

Chapter 4. Discussion

In this section we will discuss some of the characteristics of the nuclei seen in the data. We will start by looking at ^{114}Sn as it is the most abundant nucleus found in the data set. There are other residual nuclei seen in the data, the most prominent ones being ^{114}In, ^{115}In and ^{115}Cd.

We will begin by discussing the states in the ground state band and Band 1 together, as neither band represents any kind of rotational motion and is simply a collection of decays grouped and labelled as bands for simplicity [19]. Many of the yrast states of ^{114}Sn are in these two bands and the ground state is associated with a spherical shape [22]. According to Wirowski *et al.* [22], these states also make up many of the spherical states of ^{114}Sn. The 6^+, 3149-keV, state in the ground state band and the 9^-, 3510-keV, state in Band 1 are associated with neutron 2-quasiparticle excitations [7]. For example, the 9^- state is identified as a $(\nu g_{7/2} \times \nu h_{11/2})_{9^-}$ stretched state by Gerlic *et al.* [7].

Gerlic *et al.* [7] stated that in the reaction ^{116}Sn(p,t)^{114}Sn this 9^- state is seen as a doublet with a 6^+, 3470-keV, state. However we do not see a 6^+, 3470-keV, state in our data. We do see a different 6^+ state at 3149-keV in the ground state band and it has been suggested by Gerlic *et al.* [7] that it may have a configuration of $(\nu g_{7/2} \times \nu 2d_{5/2})_{6^+}$ or $(\nu g_{7/2})^{2^-}_{6^+}$. In Band 1, the 7^-, 3087-keV, state has been suggested by Gerlic *et al.* [7] to have a configuration of $(\nu g_{7/2}$ or $\nu d_{3/2}$ or $\nu d_{5/2} \times \nu h_{11/2})_{7^-}$.

The 8^- state seen in Band 2 has been identified as an isomeric state in ^{114}Sn by Van Poelgeeste *et al.* [20] and they have also measured its half-life to be $T_{1/2} = 0.35(20)$ ns. This state has also been related to a neutron quasiparticle excitation [20].

If we turn our attention to slightly higher energy levels, in Band 3 the 10^+ state at 4139 keV is assigned a configuration of $(\nu h_{11/2})^2_{10^+}$ [10] as it follow the systematic trend of the other noncollective excited states in ^{114}Sn with spins $I \leq 10$. All of these noncollective states including the 10^+ state are interpreted to be fairly pure 2-quasiparticle states [10]. Above

the 10^+ state in Band 3 lies a 12^+ level at 5180 keV, which Harada *et al.* [10] suggest could be a 2-quasiparticle excitation coupled to a 2_1^+ spherical state. Harada *et al.* [10] interpret this spherical 12^+ state as a 4-quasineutron state.

Looking now at Band 4, this is a positive-parity band, which is also known as the "Amsterdam band" and has angular momentum projection K $^{\pi}= 0^+$ [22]. This band has been observed in the even tin isotopes $^{112-118}$Sn [6]. It is associated with a prolate deformation of the nucleus with a deformation parameter of β_2=0.26 with a value of Q_0=3.49 eb [6].

This band is due to a two-particle-two-hole (2p-2h) excitation which occurs across the Z=50 closed proton shell, and has $\{\pi\frac{1}{2}^+[431]^2 \otimes \pi\frac{9}{2}^+[404]^{-2}\}_{K=0}$ as its Nilsson configuration [6]. The promotion of 2 protons across the Z=50 shell gap creates deformed 2p-2h $\pi g_{7/2}^2 g_{9/2}^{-2}$ states that are low-lying. Deformation arises as the two protons are moved from up-sloping $g_{9/2}$, high-Ω, orbitals to down-sloping $g_{7/2}$, low-Ω, orbitals. Downward-sloping orbitals are deformation-driving orbitals, such as the $g_{7/2}$ orbital at β_2=0.26. Due to the presence of 2 protons in this $g_{7/2}$ orbital, we expect to see prolate deformation occurring. This is in agreement with the previously discussed deformation of this band.

Band 4 can be better understood if we compare it with a similar band in ^{118}Sn. We expect similar shape evolution for ^{114}Sn as for ^{118}Sn because both nuclei contain structures with the same configuration and similar deformation values. Band 4 in ^{114}Sn and the Amsterdam band in ^{118}Sn have very similar energy spacings and this is consistent with similar quadrupole deformation. Total routhian surface (TRS) cranking calculations were performed by Wang *et al.* [21] for ^{118}Sn and 2 energy minima were found at zero rotational frequency. One minimum corresponds to a spherical shape with β_2=0, which is the ground state, vacuum configuration, and another minimum with β_2=0.23 corresponds to prolate deformation with a 2p-2h configuration. The TRS calculations carried out by Wang *et al.* [21], shown in Figure 23, show a good example of shape coexistence as there are 2 minima seen in the plots for rotational frequencies of 0.00 MeV, 0.10 MeV and 0.20 MeV. The minimum seen in the plot with rotational frequency of 0.50 MeV has a β_2=0.102 and a γ=60^o value, which

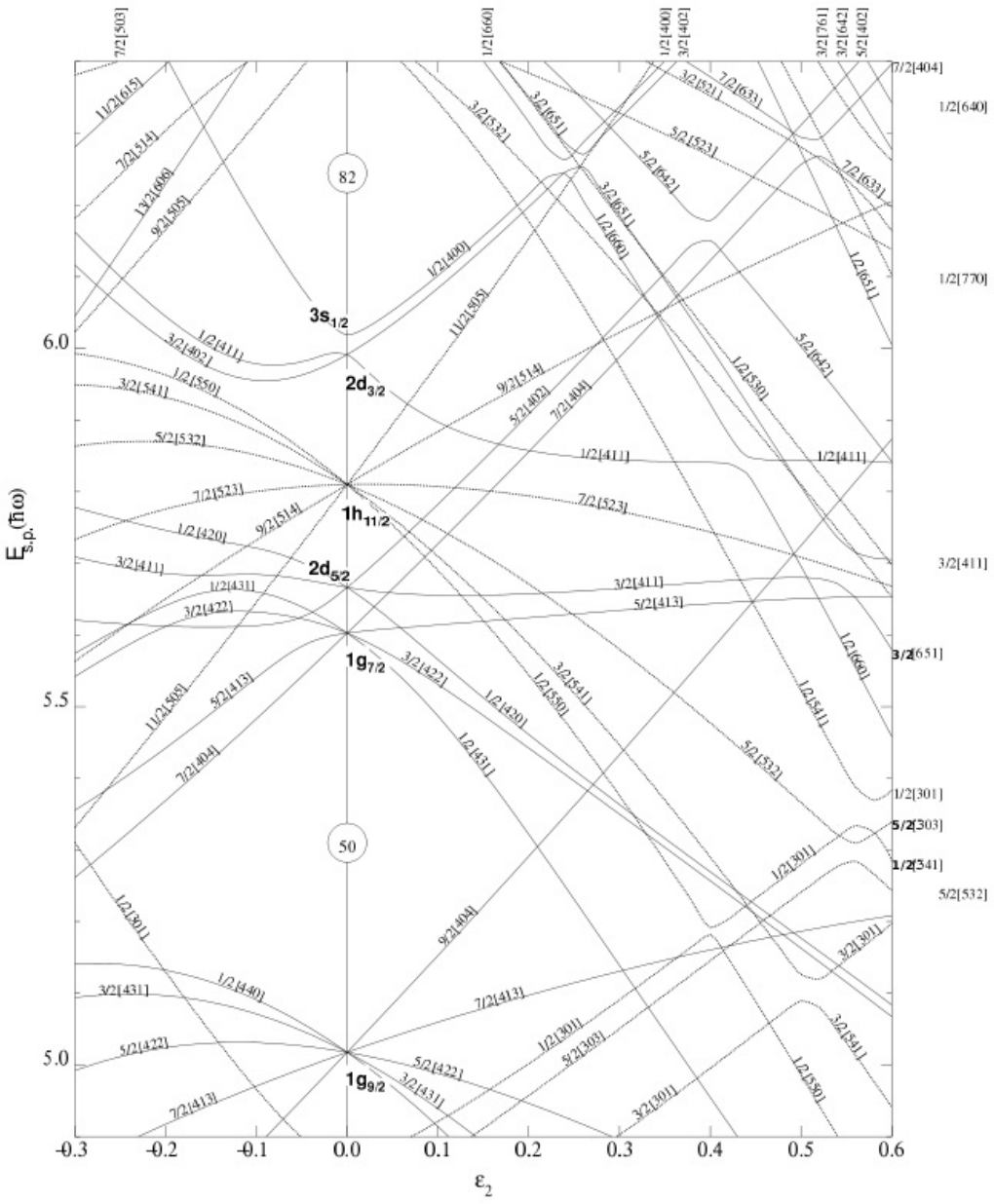

Figure 22: Nilsson diagram [5] for protons, $50 \leq Z \leq 82$ ($\varepsilon_4 = \varepsilon_2^2/6$)

corresponds to a noncollective oblate deformation [21]. If we refer to Figure 23, in ^{118}Sn at high rotational frequency above the backbending the nucleus becomes $\gamma-$soft, and we can expect a similar shape for ^{114}Sn.

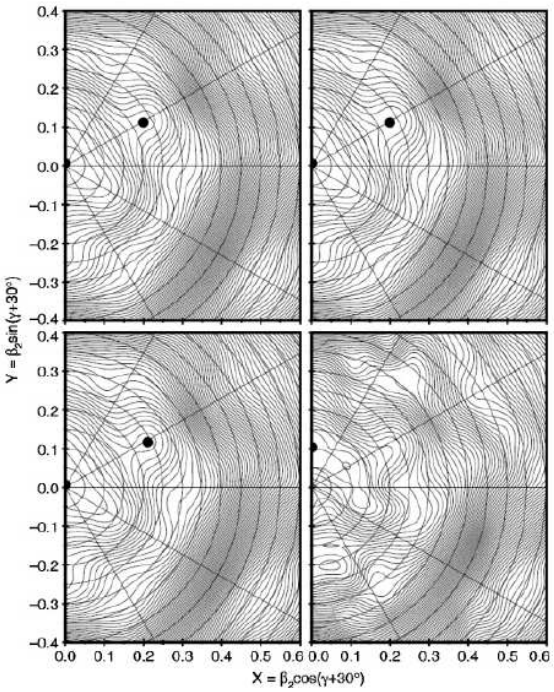

Figure 23: Total Routhian surface calculations for ^{118}Sn at $\hbar\omega$=0.00 MeV (top left), $\hbar\omega$=0.10 MeV (top right), $\hbar\omega$=0.20 MeV (bottom left) and $\hbar\omega$=0.50 MeV (bottom right). Energy contours are at 200-keV intervals [21].

Figure 24 shows the alignment i_x as a function of rotational frequency for Band 4, and we can see that the rotational alignment increases steadily with rotational frequency. This is due to the gradual rotational alignment of the $h_{11/2}$ neutrons. Figure 24 shows only observed states below the backbending.

According to Gableske *et al.* [6], in Band 4 of ^{114}Sn sharp backbending occurs in the plot of alignment versus frequency at the 12^+, 5548-keV, level caused by the alignment of two

quasineutrons $(\nu h_{11/2})^2$. However, in our data we are only able to see up to the 12^+ state and therefore do not see the levels associated with the alignment of these quasineutrons. The backbending occurs in ^{118}Sn at a frequency of 0.45 MeV while in ^{114}Sn the backbending occurs at a slightly lower frequency of 0.41MeV [21].

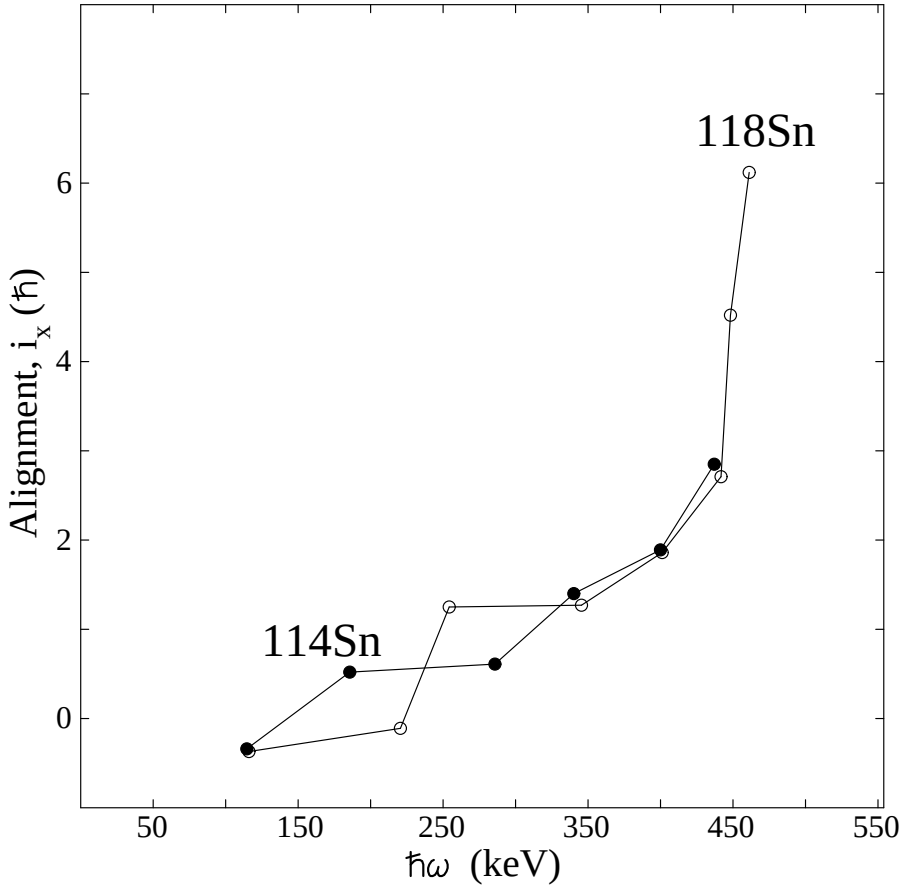

Figure 24: Experimental alignment plots for Band 4 in ^{114}Sn seen as filled circles, plotted with the alignment plot for the Amsterdam band in ^{118}Sn, hollow circles, as seen in Wang *et al.* [21]. The Harris parameters used are J_0=15 $\hbar^2$ MeV^{-1} and J_1=25 $\hbar^4$ MeV^{-3}.

Guazzoni *et al.* [8] compared results from the ^{116}Sn(p,t)^{114}Sn reaction with shell model calculations of ^{114}Sn. They compared the observed states with states predicted by the theory and found that the theoretical results match the states observed experimentally. A one-to-one correspondence between experimental energy levels and theoretical energy levels was observed up to approximately 3.5 MeV, their results suggest that the shell model could be the best available model to describe the tin isotopes [8].

Doornenbal *et al.* [4] determined the B(E2; $0_1^+ \rightarrow 2_1^+$), abbreviated to B(E2↑), value in ^{114}Sn to be 0.232(8) e^2b^2, and have stated that this value is the starting point of a deviation from a symmetric trend observed in the B(E2↑) values. This trend was observed around the N=66 neutron midshell in radioactive beam experiments of the proton rich $^{106-110}$Sn nuclei [4]. This deviation suggests a disagreement with the current shell model calculations and suggests the need for a refinement of the two-body interactions employed [4]. They suggested that further experimental studies of the Z=50 and N=50 gaps would be of vital importance. Theoretical studies of these shell gaps would also be necessary, and together the experimental and theoretical studies would shed light on the nuclear structure in the vicinity of the doubly magic ^{100}Sn [4].

Chapter 5. Conclusion

This experiment and the data collected from it has allowed several new $\gamma-$rays to be added to the decay scheme of ^{114}Sn. These additions were made via the systematic study of $\gamma-$ray coincidence data collected from the $^{114}_{48}Cd_{66}(^{3}He,3n)^{114}_{50}Sn_{64}$ two proton stripping reaction. The experiment was run with a beam energy of 25 MeV and successfully populated several new states. We were also able to assign spin and partiy to most of the new levels, as well as relocate a level that was previously placed incorrectly within the decay scheme of ^{114}Sn.

DCO analysis and polarisation anisotropy analysis were carried out on the data in order to assign spin and parity to the new levels. Some of the new states were successfully assigned spin and parity, however due to low counts the multipolarity of some of the new decays could not be determined and therefore the spin and parity of some states remain unknown. We can conclude that the DCO analysis and polarisation anisotropy analysis are useful tools used in determining the spin and parity of the states in the level scheme.

Band 4 (the Amsterdam band) was of particular interest to us as it contains a 0^+_2 excited state. The 0^+_2 exited state is sometimes observed when double-beta decay occurs. This band may therefore be able to aid in the understanding of double beta decays by paying attention to the lifetime of the 0^+_2 excited state as well as investigating the transitions into the state. The band was populated up to the 12^+, 5548-keV, state and therefore we were unable to observe any backbending in the alignment plot that is known to occur above the 12^+ state. The backbending occurs in the states above 12^+ due to the alignment of two quasineutrons $(\nu h_{11/2})^2$.

Band 4 also exhibits a strong case of shape coexistence as seen in the TRS calculations, with a β_2=0 spherical shape for the ground state vacuum configuration and a β_2=0.23 prolate deformed 2p-2h configuration for the low rotational frequencies. For rotational frequencies above 0.50 MeV, the band takes on a β_2=0.102 noncollective oblate deformation, however it is also found to be $\gamma-$soft.

The search for neutrinoless double beta decay ($\beta\beta(0\nu)$) is very important in the attempts to determine if neutrinos are in fact "Majorana Particle" or in other words are their own antiparticles. The observation ($\beta\beta(0\nu)$) would help to back up theories such as effective-field theory and grand-unification schemes. Conversely, the proof that ($\beta\beta(0\nu)$) does not occur would also help to develop these theories. Experiments such as the two proton stripping experiment may be able to add to what is known about double beta decay by studying the 0_2^+ state seen when double beta decay occurs.

Much is still unknown about double beta decays, and further dedicated half-life experiments would be needed to understand double beta decays. These studies may be able to determine the mechanism of double beta decay and in turn reveal whether or not the neutrino is indeed its own antiparticle.

This investigation into ^{114}Sn has led to a better understanding of the shapes and deformations of nuclei. The experiment and its results have also demonstrated many of the nuclear theories and analytical techniques discussed in the thesis. It has shown cases of shape coexistence discussed in the deformed shell model as well as backbending and alignment discussed in the particle rotor model. In conclusion the experiment successfully demonstrates many aspects of experimental nuclear physics and provides validity for key nuclear theories.

References

[1] F. T. III Avignone, S.R. Elliott, and J. Engel. Double Beta Decay, Majorana Neutrinos, and Neutrino Mass. *Rev.Mod.Phys.*, **80**:481–516, 2008.

[2] E. M. Bernstein, G. G. Seaman, and J. M. Palms. Coulomb excitation of ^{113}In and ^{115}In with oxygen ions. *Nuclear Physics A*, **114**(1):67–74, 1970.

[3] S. P. Bvumbi, J.F Sharpey-Schafer, S. H. Connell, S.M. Mullins, A.E. Lawrie, P. Papka, S.N.T Majola, O. Shirinda, P. Datta, P. Jones, A. Minkova, J. Timar, B. Nyako, L.L. Riedenger, I. Ragnarsson, P.E. Garrett, and L. Bianco. *The structure of excited states seen in double beta decay.* SAIP presentation, University of Pretoria, 12 Jul 2012.

[4] P. Doornenbal, P. Reiter, H. Grawe, H. Wollersheim, P. Bednarczyk, L. Caceres, J. Cederkäll, a. Ekström, J. Gerl, M. Górska, a. Jhingan, I. Kojouharov, R. Kumar, W. Prokopowicz, H. Schaffner, and R. Singh. Enhanced strength of the $2_1^+ \rightarrow 0_{g.s.}^+$ transition in ^{114}Sn studied via Coulomb excitation in inverse kinematics. *Physical Review C*, **78**(3):031303, September 2008.

[5] R. B. Firestone, V. S. Shirley, C. M Baglin, S. Y. Frank Chu, and J. Zipkin. *Table of Isotopes*, volume II. John Wiley & Sons, Inc., 1999.

[6] J. Gableske, A. Dewald, H. Tiesler, M. Wilhelm, T. Klemme, O. Vogel, I. Schneider, R. Peusquens, S. Kasemann, K.O. Zell, P. von Brentano, P. Petkov, D. Bazzacco, C. Rossi Alvarez, S. Lunardi, G. de Angelis, M. de Poli, and C. Fahlander. Collectivity of the intruder bands in ^{114}Sn. *Nuclear Physics A*, **691**:551–576, 2001.

[7] E. Gerlic, J. Guillot, J. Langevin-Joliot, J. Van de Wiele, S. Gales, G Duhamel, G Perrin, CP Massolo, and M Sakai. Stretched high-spin two-neutron-hole states in ^{206}Pb and ^{114}Sn via the (p,t)reaction at 168MeV. *Physical Review C*, **39**(6), 1989.

[8] P. Guazzoni, L. Zetta, a. Covello, a. Gargano, G. Graw, R. Hertenberger, H.-F. Wirth, and M. Jaskola. High-resolution study of the ^{116}Sn(p,t) reaction and shell model structure of ^{114}Sn. *Physical Review C*, **69**(2):024619, February 2004.

[9] E. Gueorguiva-Lawrie. Rhodes University Nuclear Physics Honours 2012 Part II. *Lecture Notes*, 2011.

[10] H. Harada, M. Sugawara, H. Kusakari, H. Shinohara, Y. Ono, K. Furuno, T. Hosada, M. Adachi, S. Matsuki, and N. Kawamura. High-spin states in ^{114}Sn. *Physical Review C*, (1):132–138.

[11] P. Jones and J.F. Sharpey-Schafer. Research Proposal to the iThemba LABS: Physical Sciences Research Programme on the SSC Facility. **Experiment PR206**:Two proton stripping at the Z=50 closed proton shell, 2012.

[12] K.S. Krane and D. Halliday. *Introductory nuclear physics*. Wiley, New York, 1987.

[13] S.G. Nilsson and I. Ragnarsson. *Shapes and Shells in Nuclear Structure*. Cambridge University Press, 1995.

[14] E.S. Paul. Liverpool NSG Postgraduate Lectures. *Liverpool University unpublished lecture notes*.

[15] V. Pucknell. *MIDAS 4.7*. Science & Technologies Facilities Council Nuclear Physics Group, Saltburn-by-the-Sea, Cleveland, 2003.

[16] D.C. Radford. ESCL8R and LEVITSR: Software for interactive graphical analysis of HPGe coincidence data sets. *Nucl. Instrum. Methods A*, **361**(297), 1995.

[17] D.G. Roux, K.R. Henninger, R.A. Bark, S. Bvumbi, E.A. Gueorguieva-Lawrie, J.J. Lawrie, S.M. Mullins, S.H.T. Murray, S.S. Ntshangase, L.P. Masiteng, and O. Shirinda. In-beam spectroscopy of ^{72}Ge. *The European Physical Journal A*, **48**(7), 2012.

[18] M. Schimmer, S. Albers, A. Dewald, A. Gelberg, R. Wirowski, and P. von Brentano. On negative-parity intruder bands in ^{114}Sn. *Nuclear Physics A*, **539**(3):527–546, March 1992.

[19] M. Schimmer, R. Wirowski, and P. von Brentano. The valence mirror nuclei ^{114}Sn and ^{146}Gd. *Nuclear Physics A*, **569**(3):458–468, March 1994.

[20] A. Van Poelgeest, J. Bron, W.H.A. Hesselink, K. Allaart, J.J.A. Zalmstra, M.J. Uitzinger, and H. Verhuel. Neutron excitations in even mass Sn nuclei. *Nuclear Physics A*, **346**(1-2):70–92, September 1980.

[21] S. Y. Wang, D. P. Sun, B. T. Duan, X. L. Ren, B. Qi, X. X. Zhu, F. Z. Lv, C. Liu, C. J. Xu, J. Meng, H. Hua, F. R. Xu, Z. Y. Li, S. Q. Zhang, Y. Shi, J. M. Yao, L. H. Zhu, X. G. Wu, G. S. Li, Y. Liu, X. Q. Li, Y. Zheng, L. L. Wang, and L. Wang. Coexistence of collective and noncollective structures in ^{118}Sn. *Physical Review C*, **81**(1):017301, January 2010.

[22] R. Wirowski, M. Schimmer, L. Eßer, S. Albers, and K.O. Zell. γ-spectroscopy of ^{114}Sn with the OSIRIS-cube-spectrometer. *Nuclear Physics A*, **586**(3):427–444, 1995.

[23] S. S. M. Wong. *Introductory nuclear physics*. Prentice-Hall, Englewood Cliffs, N.J., 1990.